Response of a Simulated Hurricane to Misalignment Forcing Compared to the Predictions of a Simple Theory

David A. Schecter*

NorthWest Research Associates, Boulder, CO, USA 80301

Submitted to Journal of the Atmospheric Sciences, May 23, 2014; revised September 16, 2014; updated with minor edits December 8, 2014

*Corresponding author address: NorthWest Research Associates, 3380 Mitchell Lane, Boulder, CO, USA, 80301. E-mail: schecter@nwra.com

Abstract

This paper compares the tilt dynamics of a mature tropical cyclone simulated with a conventional cloud model to reduced modeling results and theoretical predictions. The primary experiment involves a tropical cyclone of hurricane strength on the f-plane exposed to a finite period of idealized misalignment forcing. A complementary experiment shows how the vortex responds to the same forcing when moisture and symmetric secondary circulation (SSC) are removed from the initial condition. It is found that the applied forcing excites a much stronger tilt mode in the dry nonconvective vortex than in the moist convective hurricane. The evolution of tilt in both experiments agrees reasonably well with a simple linear response theory that neglects the SSC and assumes moisture merely reduces static stability in the vortex core. An additional experiment with suspended cloud water but no substantial SSC supports the theoretical notion that reduction of static stability is sufficient to inhibit the excitation of a tilt mode. However, there is some discrepancy between theory and details of asymmetric convection in the eyewall region of the simulated hurricane. Moreover, a final experiment without moisture but with an artificially maintained secondary circulation suggests that the SSC has a non-negligible role in reducing tilt. Diagnosis of the primary hurricane simulation further illustrates how the SSC has discernible influence over misalignment at least in the eyewall. Sensitivity of tilt dynamics to the azimuthally averaged vortex structure is briefly addressed.

1. Introduction

There has yet to emerge a complete understanding of the mechanisms that drive a tropical cyclone (TC) toward a state of vertical alignment. It is of interest to elucidate the alignment mechanisms, and the conditions that improve their effectiveness, because tilted TCs are often weaker than their upright counterparts [e.g. Riemer et al. 2010; Frank and Ritchie 2001; DeMaria 1996]. This paper explicitly demonstrates some of the merits and deficiencies of a recently advanced theory of tilt dynamics.

1.1 Review of the Theory at Issue

The literature contains a number of articles on the tilt dynamics of nonconvective vortices in a stably stratified atmosphere. Some of these articles discuss how vortices resist tilting under sustained vertical wind-shear [Jones 1995-2004; Vandermeirsh et al. 2002; Reasor et al. 2004 (R04)]. Others focus on the decay of tilt in the absence of external forcing [Polvani 1991; Viera 1994; Reasor and Montgomery 2001 (RM01); Schecter et al. 2002 (S02); Schecter and Montgomery 2003 (SM03); Jones et al. 2009]. It has been shown that TC-like vortices commonly have mechanisms to counter tilt without diabatic processes driving a mean secondary circulation to potentially assist. It has also been shown that the effectiveness of such mechanisms can depend on details in the spatial distribution of potential vorticity (PV).

In a simple but common scenario, the vertical misalignment of PV in a nonconvective vortex is dominated by a special vortex Rossby (VR) wave, here called the Principal Tilt Mode (PTM). The PTM is usually damped by depositing wave activity into an outer critical layer, where the mode is resonant with the fluid rotation [S02; SM03]. Sensitivity of critical layer damping to details partly accounts for variable tilt dynamics in seemingly similar vortices. Nevertheless, PTMs are found to follow some basic "rules of thumb." Weaker static stability or greater inertial stability in the vortex core tends to increase the natural precession frequency and damping rate of the PTM. These changes are thought to help reduce the excitability of the PTM and thereby enhance the resistance of the vortex to slow misalignment forcing, such as that related to ambient vertical wind-shear. Note that if the PTM is very strongly damped, the weak tilt created by forcing may largely consist of ordinary continuum modes and degenerate into sheared VR waves [RM01;R04]. The residual alignment mechanism may then involve the spiral windup and outward propagation of such waves.

Of course, PTMs are not always damped. Appendix A discusses various conditions under which PTMs may persist or spontaneously grow without forcing. Furthermore, there may be additional shear-flow instabilities independent of the PTM that frustrate vertical alignment [cf. Nolan et al. 2001; Smith and Rosenbluth 1990]. Such instabilities are often overlooked in simplified studies by choosing a vortex in which they develop slowly or do not exist. The relevance of this choice is questionable for the study of intense TCs.

Perhaps the most pressing concern regarding the PTM paradigm of tilt dynamics is the simplified manner in which moisture has been incorporated into the theory. The PTM paradigm is largely based on a simple linear model that treats moisture merely as a local reduction of static stability [Schecter and Montgomery 2007 (SM07); R04]. Because reducing static stability tends to lessen the excitability of a PTM, this model has a mechanism for moisture to inhibit tilt. Such moisture-induced inhibition is qualitatively consistent with earlier computational studies such as Wang and Holland 1996. However, the explanation provided by the simple model has not been thoroughly tested. The simple model neglects how tilt is influenced by deep convective transport by the diabatically maintained symmetric secondary circulation (SSC). The simple model also neglects the effects of surface fluxes and boundary layer processes on the asymmetric convection that is coupled to the behavior of a PTM. Finally, the simple model overlooks nonlinear and stochastic elements of deep convection.

One might infer from a number of quasi-realistic TC simulations in the literature that the features of moist convection neglected by current theory have some influence on the behavior of tilt [e.g. Rogers et al. 2003; Wong and Chan 2004; Braun et al 2006; Zhang and Kieu 2006; Braun and Wu 2007; Davis et al. 2008; Zhang and Tao 2013]. The same inference might be drawn from recent efforts to understand the observed relationship between convective asymmetry and tilt in real TCs exposed to ambient vertical wind-shear [e.g. Reasor and Eastin 2012; Reasor et al. 2013]. However, the merits and shortcomings of current theory have not been fully clarified.

1.2 Objectives and Overview of the Present Study

The main objective of the present study is to directly test the assumptions and predictions of the simple linear theory (SLT) of tilt dynamics described above. Assessment of the SLT will be based on computational experiments with a conventional cloud model (CM), in which a TC of hurricane strength is exposed to a period of idealized misalignment forcing and then released to evolve freely with time. The primary experiment (E1) is designed to include all relevant physical processes. A second experiment (E2) carefully removes all moisture and the SSC from the vortex before the forcing is applied. A third experiment (E3) removes the SSC but includes suspended cloud droplets and the attendant reduction of static stability inside the vortex. A fourth experiment (E4) removes moisture but maintains the SSC through an artificially distributed heat source.

Comparison of the primary hurricane experiment (E1) to the nonconvective dry vortex experiment (E2) will confirm that moist convection severely inhibits the development of tilt and the excitation of the PTM. Moreover, the evolution of tilt in both experiments will be found to agree reasonably well with explicit predictions of the SLT. The outcome of E3 will support the theoretical notion that reduction of static stability by cloud water is sufficient to inhibit the excitation of a PTM. However, some discrepancies will be found between the SLT and details of asymmetric convection in the eyewall region of the E1-hurricane. Moreover, E4 will provide evidence that the SSC has a non-negligible role in reducing tilt. Diagnosis of E1 will further illustrate how the SSC has discernible influence over misalignment at least in the eyewall.

For good measure, experiments E1 and E2 will be repeated with a slightly more intense and contracted vortex. The results will confirm various differences with the original experiments predicted by the SLT.

1.3 Outline of the Remaining Sections

The remainder of this article is organized as follows. Section 2 describes the computational setup for each CM experiment. Section 3 presents the relevant SLT. Section 4 presents the results of the CM experiments. Section 5 summarizes the main findings of this study. The appendices supplement the main text with some notable technical details.

2. Setup of the Numerical Experiments

2.1 Configurations of the Cloud Model

The numerical simulations are conducted with the Regional Atmospheric Modeling System (RAMS 6.0), which is maintained and distributed to the public by ATMET LLC. RAMS is a conventional weather research model with a variety of options for parameterizing cloud microphysics, radiation, subgrid turbulent transport, and surface-fluxes [Cotton et al. 2003]. Certain parts of the physics modules were simplified for this particular study, as described below.

The primary experiment (E1) involves a well-developed hurricane. For this experiment, RAMS is configured with single-moment warm-rain microphysics [Walko et al. 1995] and a longwave radiation scheme that neglects the effects of condensate [Mahrer and Pielke 1977]. The subgrid turbulence parameterization is anisotropic, with the vertical component based on a local Smagorinsky [1963] closure. The standard RAMS enhancement of the vertical mixing coefficient in regions of moist instability is removed to limit the impact of diffusion on vertical alignment (see section 4.7). The horizontal mixing coefficient is effectively constant and barely large enough to prevent excessively strong grid-scale fluctuations in the convective core of the vortex. The ratio of momentum to scalar mixing coefficients is 1/3.

Although RAMS includes a sophisticated module for computing surface-fluxes [Walko et al. 2000; Louis 1979], E1 uses a simpler scheme that is adequate for idealized hurricane simulations. In particular, the following equations are used for the surface-fluxes of horizontal momentum (τ_{ux},τ_{uy}), sensible heat (τ_θ) and moisture (τ_q):

$$\begin{aligned} \tau_{ux} &= -C_D\,|\mathbf{u}_+|\,u_{x+}, & \tau_{uy} &= -C_D\,|\mathbf{u}_+|\,u_{y+}, \\ \tau_\theta &= C_E\,|\mathbf{u}_+|\,(\theta_s-\theta_+), \quad \text{and} & \tau_q &= C_E\,|\mathbf{u}_+|\,(q_{s*}-q_+), \end{aligned} \tag{1}$$

in which $\mathbf{u} \equiv (u_x, u_y)$ is horizontal velocity, θ is potential temperature, and q is the water vapor mixing ratio. The variables θ_s and q_{s*} denote sea-surface values for θ and the saturation mixing ratio. The subscript '+' indicates that the variable is evaluated at the first vertical grid point above sea-level. The dimensionless surface-exchange coefficients are obtained from a capped modification of Deacon's formula,

$$C_D = C_E = 1.1\times10^{-3} + 4\times10^{-5}\min\left(|\mathbf{u}_+|\,,30\right), \tag{2}$$

with $|\mathbf{u}_+|$ given in m s^{-1}. The sea-surface temperature is held constant at a low value of 23 ^{o}C, which prevents eyewall replacement cycles during the experiment.

The computational domain is a periodic f-plane at 20^o N. The value of the Coriolis parameter f is therefore 5×10^{-5} s^{-1}. The fields are evolved on 3 nested grids spanning 567, 1235 and 4500 km in the east-west and north-south directions. The corresponding horizontal grid increments are 1.67, 5 and 15 km. The vertical mesh is the same for all grids and is stretched with height z over 80 increments up to $z = 31$ km. The vertical grid spacing is 60 m near the ground, 140 m at $z = 2$ km, and 500 m for $z > 10$ km. Rayleigh damping is applied near the upper boundary to eliminate vertically propagating waves that would otherwise remain artificially trapped in the system. The damping rate increases linearly with z, from 0 at $z = 23$ km to 0.003 s^{-1} at the model top.

The reference state of the atmosphere used by the dynamical core of RAMS in E1 is similar to the Jordan mean sounding (JMS) for hurricane season in the West Indies [Jordan 1958]. The actual domain-averaged sounding that develops in the process of creating the hurricane differs from the JMS as described in appendix B.

Experiments E2-E4 (introduced in section 1.2) have some basic configurational similarities with E1. The grids are equivalent to those of E1, as are the settings for turbulent transport and Rayleigh damping. The atmospheric reference states are the same, but without moisture in E2 and E4. That said, the configurational differences between E2-E4 and E1 summarized in Table 1 are essential. In each case, the radiation scheme is switched off. All surface fluxes are eliminated in experiments E2 and E3, whereas only the surface momentum flux is retained (explicitly) in E4. Experiment E2 has no moisture and no artificial representation of diabatic cloud processes. The simplified methods for modeling cloud processes in E3 and E4 are explained below.

Experiment E3 includes moisture only in the forms of vapor and suspended cloud droplets. Through minor code modifications, the cloud droplets in E3 are given zero terminal velocity. Experiment E4 artificially approximates diabatic cloud processes (combined with surface heat exchange and radiation) with a fixed source term in the prognostic θ-equation of the form

$$\dot{\theta}_{src}(r, z) = u_{p0}\, \partial_r \theta_{p0} \;+\; w_{p0}\, \partial_z \theta_{p0}. \tag{3}$$

Here and hereafter, r, φ and z denote radius, azimuth and height in a cylindrical coordinate system. The symbols ∂_x and ∂_{xx} (used later) concisely denote the first and second partial derivatives with respect to the generic variable x. In general, u, v and w denote radial, azimuthal and vertical velocity fields. All variables having the subscript $p0$ correspond to the initial axisymmetric hurricane of the primary CM experiment (E1). The heat source given by the right-hand side (rhs) of Eq. (3) is that required to maintain $\theta = \theta_{p0}(r, z)$ with a secondary circulation given by $u = u_{p0}(r, z)$ and $w = w_{p0}(r, z)$. It is used here to drive an approximately steady mean secondary circulation in a dry simulation. Unlike E3, small perturbations in E4 do not experience a reduced buoyancy restoring force through phase transitions of cloud water.

2.2 Initialization

Figure 1 depicts the initial axisymmetric state of the hurricane in E1, obtained from the azimuthally averaged fields of a mature system in a preliminary RAMS simulation described in appendix B. Figure 1a shows the azimuthal velocity v and the perturbation of potential temperature θ from its z-dependent value at $r \approx 2200$ km. The vortex is seen to exhibit classic warm core structure. The absolute maximum of v is 61.2 m s^{-1} at $r_{max} = 90$ km and $z_{max} = 0.95$ km. The large size of the storm is helpful for resolving small misalignments on the computational grid used for this study. Further discussion of the storm scale is deferred to section 2.4. Figure 1b shows the overturning secondary circulation in the vortex core. The maximum of w in the eyewall updraft is 2.9 m s^{-1}. Figure 1c shows contours of saturation pseudoadiabatic entropy s_{p*} [Bryan 2008] and absolute angular momentum $\mathcal{L} \equiv rv + fr^2/2$ superposed on a plot of the water vapor mixing ratio q. The state of the eyewall is reasonably close to slantwise convective neutrality, in which the contours of s_{p*} and $\mathcal{L}$ are congruent [cf. Emanuel 1986]. Figure 1d shows contours of q_r superposed on a plot of $q_r + q_c$, in which q_r and q_c respectively represent the rain and cloud droplet mixing ratios.

The dry baroclinic vortex in E2 is initialized with no secondary circulation and v approximately matching that of the initial hurricane of E1. The only notable difference in the primary circulation is that v does not vary with height between the sea-surface and z_{max}. To elaborate, the initial conditions for v, θ and the perturbation Exner function Π (the prognostic pressure variable in RAMS) correspond to the azimuthally averaged end-state of a 24-h relaxation procedure. The relaxation procedure is to nudge the velocity field toward its intended state with a damping rate of 0.5 h^{-1} while letting θ and Π freely adjust. At the beginning of the procedure, v, θ and Π are matched to the initial conditions of E1, whereas u and w are set to their intended values of zero.

The cloudy vortex in E3 is initialized with no secondary circulation and v approximately matching that of the initial vortex in E2. The precise initial conditions for v, θ, and Π correspond to the azimuthally averaged end-state of a 24-h relaxation procedure analogous to that of E2, but with unnudged moisture fields (q and q_c) included. Following the relaxation procedure, the cloud droplet mixing ratio q_c is mostly removed outside the eyewall and outflow regions defined by the E1-hurricane. In the remaining cloud, q_c is reset to approximately 5 g kg^{-1} and the edges are smoothed. The distribution of q obtained from the relaxation procedure is then adjusted where necessary to ensure saturation where $q_c > 0$ and subsaturation where $q_c = 0$. The ice-liquid potential temperature (the prognostic heat variable in moist RAMS simulations) is initialized in accordance with the distributions of θ, Π and q_c. Section 3.2 and appendix C further discuss the cloud distribution in E3 and how it theoretically affects static stability in the vortex.

The initial conditions of E4 are obtained from a distinct relaxation procedure. The relaxation period starts with u, v, w, θ and Π matched to the initial conditions of E1. The system then evolves for 24 hours under the thermal forcing of Eq. (3) with no additional nudging. The azimuthally averaged end-state is used to initialize E4.

Figure 2a demonstrates that the mass-weighted z-averaged relative vorticity (ζ) distributions in E1-E4 are initially the same to within a reasonable approximation. However, the preliminary relaxation in E2 and E3 alters the initial distribution of θ. The modest change of θ combined with the removal of secondary circulation and vertical shear below z_{max} affects some details of the PV distribution in the vortex core. The PV in E4 also differs somewhat from that of E1 owing to a variety of modifications affecting the relaxed state, such as the removal of water mass.

Figures 3a-3d show how the main CM experiments subtly differ in their initial r-θ profiles of dry isentropic PV, defined by

$$\mathrm{PV}_\theta \equiv (\zeta_\theta + f)/\sigma, \tag{4}$$

in which $\zeta_\theta \equiv [\partial_r(rv) - \partial_\varphi u]/r \to \partial_r(rv)/r$, $\sigma \equiv -\partial_\theta p/g$, and $g = 9.8$ m s^{-2} is the gravitational acceleration. The r and φ derivatives are here taken at constant θ, and the φ derivative vanishes owing to axisymmetry of the initial vortex. The lower bound of θ on each plot corresponds to the maximum of θ at $z = 30$ m. The upper bound corresponds to the minimum of θ at $z = 14$ km. It seems doubtful that subtle PV differences in E1-E4 change tilt dynamics as much as the principal configurational differences summarized in Table 1, but they are worth keeping in mind.

2.3 Forcing Applied to Create Tilt

In each CM experiment, the vortex is misaligned by adding an acceleration of the form

$$\dot{\mathbf{v}}_a = -\frac{2\pi n A}{\tau}\cos\left(\frac{\pi z}{H}\right)\left[\cos\left(\frac{2\pi n t}{\tau}\right)\hat{\mathbf{x}} + \sin\left(\frac{2\pi n t}{\tau}\right)\hat{\mathbf{y}}\right], \qquad z < 3H/2, \tag{5}$$

to the rhs of the horizontal momentum equation over a time-period τ. The acceleration vector $\dot{\mathbf{v}}_a$ is horizontally uniform, changes sign in the middle troposphere, and rotates cyclonically with time. The unit vectors $\hat{\mathbf{x}}$ and $\hat{\mathbf{y}}$ in the definition of $\dot{\mathbf{v}}_a$ respectively point eastward and northward. Unless stated otherwise, the parameter settings are $A = 1$ m s^{-1}, $n = 2$, $H = 12.5$ km and $\tau = 2\pi/f = 35.1$ h. Setting H to the approximate depth of the vortex ensures that the top-half and bottom-half of the vortex experience opposite horizontal forcing. By equating τ to one inertial period, the environmental air mass theoretically returns to a state of rest once the forcing stops (in the absence of frictional dissipation). In other words, the residual ambient shear-flow is minimized and the vortex evolves freely for $t > \tau$. Low frequency forcing relative to the angular velocity of the vortex should also prevent the excitation of substantial inertia-gravity waves in its core.

One positive aspect of the vortex perturbation procedure used here is that it facilitates study of both forced and freely evolving tilt in the same experiment. Although the applied forcing $\dot{\mathbf{v}}_a$ may be unnatural, it is deemed acceptable for investigating the fundamental applicability of the SLT to hurricanes. If the SLT fails to explain the response of a simulated hurricane to this artificial forcing, it will most likely fail to explain the response to natural forcing for similar reasons. The basic methodology developed in the following sections for evaluating the SLT can be readily extended to future experiments on tilt maintained by static ambient wind shear.

2.4 Sensitivity Experiments

To help understand the generic and peculiar aspects of the primary CM experiments, E1 and E2 will be repeated with modified initial conditions. The modified experiments are labeled E1-c and E2-c. The initial condition of E1-c consists of the φ-averaged fields of E1, averaged over the time interval $69 \leq t \leq 71$ h. Figure 2b depicts the radially contracted relative vorticity distribution during this time period. The vorticity is seen to have a deeper central deficit and a greater peak value than at the beginning of E1. The absolute maximum of v is 71.2 m s^{-1} at $r_{max} = 72$ km and $z_{max} = 0.95$ km. The initial condition for E2-c is obtained as for E2, but with v (above z_{max}) corresponding to the initial state of E1-c.

Note that both the original and contracted vortices have uncommonly large values of r_{max} and aspect ratios (r_{max}/H) that are somewhat exaggerated. Nevertheless, they are dynamically similar to real hurricanes in having Rossby numbers that satisfy $Ro \equiv v_{max}/r_{max}f \gg 1$

and dry Froude numbers that satisfy $Fr \equiv \pi v_{max}/NH \sim 1$. Here, v_{max} is the maximum azimuthal wind speed and $N \approx 0.01$ s^{-1} is the dry Brunt-Väisälä frequency.

3. Simple Linear Theory

The following presents specific theoretical results required to compare the SLT to the CM experiments. The results are preceded by a brief description of the perturbation equations on which the SLT is based.

3.1 The Linearized Primitive Equations

The theory at issue neglects vertical variation and secondary circulation in the basic state of the vortex, and treats the tilt as a small hydrostatic perturbation [cf. R04; Schecter and Montgomery 2004 (SM04)]. A Boussinesq approximation is used to facilitate calculations. The perturbation equations are formulated using the pressure-based pseudoheight of Hoskins and Bretherton 1972 [HB72] as the vertical coordinate z. For the purpose of comparing theoretical results to the CM experiments, it is assumed that z and $w \equiv Dz/Dt$ approximately equal the genuine height and vertical velocity [HB72]. Here and elsewhere D/Dt denotes the material derivative.

The basic state of the vortex satisfies gradient-wind and hydrostatic balance. It is characterized by the azimuthal velocity $\bar{v}(r)$ and the following related fields: $\bar{\Omega} \equiv \bar{v}/r$, $\bar{\zeta} \equiv r^{-1}d(r\bar{v})/dr$, $\bar{\xi} \equiv 2\bar{\Omega} + f$ and $\bar{\eta} \equiv \bar{\zeta} + f$. The choices for $\bar{v}$ will be addressed in section 3.2.

The azimuthal velocity perturbations considered here are of the form

$$v' = \hat{v}(r,t)\cos(\pi z/H)e^{i\varphi} + c.c.,$$

in which the prime denotes a deviation from the basic state, the hat denotes a time-dependent radial wavefunction, and *c.c.* denotes the complex conjugate of the term to the left. The azimuthal and vertical wavenumbers are respectively set to 1 and π/H for consistency with the misalignment force in Eq. (5). The perturbations of u and the geopotential ϕ have the same form as v'. The pseudo vertical velocity perturbation has the form $w' = \hat{w}(r,t)\sin(\pi z/H)e^{i\varphi} + c.c.$, and similarly for θ'. It follows that $w' = \theta' = 0$ at $z = 0$ and $z = H$.

The linearized radial and azimuthal velocity equations are written

$$\begin{aligned} \partial_t \hat{u} &= -i\bar{\Omega}\hat{u} + \bar{\xi}\hat{v} - \partial_r\hat{\phi} + \hat{F}^u, \\ \partial_t \hat{v} &= -i\bar{\Omega}\hat{v} - \bar{\eta}\hat{u} - i\hat{\phi}/r + \hat{F}^v. \end{aligned} \tag{6}$$

The variables $\hat{F}^u$ and $\hat{F}^v$ are the azimuthal Fourier coefficients of the radial and azimuthal misalignment forces [divided by $\cos(\pi z/H)$] extracted from the rhs of Eq. (5).[1] The potential temperature equation may be written

$$\partial_t \hat{\theta} = -i\bar{\Omega}\hat{\theta} - \Upsilon_b N^2 \theta_{ref}\hat{w}/g, \tag{7}$$

in which θ_{ref} is the reference value of θ (say 300 K). The dry Brunt-Väisälä frequency N is set equal to 0.01 s^{-1} in close agreement with the CM experiments. The function $\Upsilon_b(r)$ is assumed to have values between 0 and 1 and theoretically accounts for the reduction of static stability (N^2) in cloudy air [cf. SM07; Durran and Klemp 1982]. Hydrostatic balance and mass continuity take the forms

$$\hat{\phi} = -\left(gH/\pi\theta_{ref}\right)\hat{\theta} \quad \text{and} \quad \hat{w} = -H\left[\partial_r(r\hat{u}) + i\hat{v}\right]/\pi r. \tag{8}$$

When integrating the above system of equations, radial derivatives at the outer bound-

[1]In other words, $\hat{F}^u = \varepsilon^{-1}\int_0^{2\pi} d\varphi \left(\hat{\mathbf{r}}\cdot\dot{\mathbf{v}}_a e^{-i\varphi}\right)$ and $\hat{F}^v = \varepsilon^{-1}\int_0^{2\pi} d\varphi \left(\hat{\boldsymbol{\varphi}}\cdot\dot{\mathbf{v}}_a e^{-i\varphi}\right)$, in which $\hat{\mathbf{r}}$ and $\hat{\boldsymbol{\varphi}}$ are the radial and azimuthal unit vectors, and $\varepsilon \equiv 2\pi\cos(\pi z/H)$.

ary ($r_b = 8000$ km) are computed with backward differencing. Linear damping is applied after the forcing period in a sponge ring extending approximately 750 km inward from r_b.

The general description of a perturbation will involve consideration of its vorticity $\zeta' \equiv [\partial_r(rv') - \partial_\varphi u']/r$ and divergence $\chi' \equiv [\partial_r(ru') + \partial_\varphi v']/r$. The corresponding r-t wavefunctions are denoted $\hat{\zeta}$ and $\hat{\chi}$. The description will also involve consideration of the two components of the angular pseudomomentum density $\mathcal{J} \equiv \mathcal{J}^{PV} + \mathcal{J}^{v\phi}$, defined by

$$\begin{aligned}\mathcal{J}^{PV} &\equiv -\frac{1}{2\pi H}\int_0^{2\pi}\int_0^H d\varphi dz \frac{r(Q')^2}{2d\bar{\zeta}/dr} \;=\; -\frac{r|\hat{Q}|^2}{2\;d\bar{\zeta}/dr} \quad \text{and} \\ \mathcal{J}^{v\phi} &\equiv -\frac{1}{2\pi H}\int_0^{2\pi}\int_0^H d\varphi dz \frac{r}{\Upsilon_b N^2}\partial_z\phi'\partial_z v' \;=\; -\frac{r\pi^2}{\Upsilon_b N^2 H^2}\Re\left[\hat{v}\hat{\phi}^*\right].\end{aligned} \tag{9}$$

Here, the asterisk denotes the complex conjugate, $\Re[\ldots]$ denotes the real part of the quantity in square brackets, and $Q' \equiv \zeta' + \bar{\eta}\partial_{zz}\phi'/\left(\Upsilon_b N^2\right)$ is the pseudo PV perturbation. Without forcing, $\partial_t Q' + \bar{\Omega}\partial_\varphi Q' = -u' d\bar{\zeta}/dr$ and $\partial_t \mathcal{J} = \partial_r\left(r^2\Re[\hat{u}\hat{v}^*]\right)/r$. The preceding equations for Q' and $\mathcal{J}$ are derived as for the particular case of dry vortices ($\Upsilon_b = 1$) in SM04.

3.2 Tangential Wind and N^2-Reduction Profiles Relevant to the CM Experiments

Table 2 summarizes the specific versions of the preceding linear model used to help predict and explain the outcomes of the CM experiments. All members of the subset {L1-1, L1-2, L2, L3-1, L3-2} have the same tangential wind profile. The azimuthal velocity $\bar{v}$ is obtained by inverting an analytic approximation of the initial vertical vorticity of E1-E4. The functional form of the approximation is depicted by the gray curve in Fig. 2a and is given by $\bar{\zeta}^0$ in Eq. (D1) of appendix D. Members of {L1-c1, L1-c2, L2-c} share a wind profile corresponding to the initial conditions of E1-c and E2-c. Here $\bar{v}$ is obtained from $\bar{\zeta}^c$, whose functional form is depicted by the gray curve in Fig. 2b and is given by Eq. (D2).

Different versions of the linear model sharing the same wind profile are distinguished by their moisture parameterizations. For L2 and L2-c, the vortex is dry and $\Upsilon_b = 1$.

For L1-1 and L1-2, Υ_b is based on the distribution of cloud water in E1. First, Eq. (32) of SM07 is used to estimate a two-dimensional N^2-reduction factor $\Upsilon(r, z)$ [Fig. 4a]. The time-average appearing in the SM07 formula for Υ is taken over the forcing period $0 \le t \le \tau$. The lowest values of Υ tend to occur in regions of substantial cloud coverage. Second, Υ is vertically averaged between 30 m and 12.3 km above sea-level. The result is here called the *raw estimate* of Υ_b. For L1-1, Υ_b is equated to an analytic approximation of the raw estimate denoted $\Upsilon_b^{E1}(r; \gamma)$, in which $\gamma = 1$ [cf. Eq. (D3)].

The justification for deriving Υ_b from Υ is admittedly questionable, because the SM07-theory formally applies to very small perturbations in non-precipitating vortices. The simplification from a moist-baroclinic vortex to a moist-barotropic vortex raises additional concerns. Approximate slantwise convective neutrality could necessitate lowering Υ_b to a magnitude much less than its raw estimate in the eyewall region of the vortex. Such further reduction of N^2 is in L1-2, where $\Upsilon_b = \Upsilon_b^{E1}$ with $\gamma = 2.2$. Figure 4b shows the raw estimate of Υ_b and the two variants of Υ_b^{E1} under consideration. The better variant for emulating the tilt dynamics of E1 is determined *a posteriori*.

For L1-c1 and L1-c2, Υ_b is modeled after the cloud coverage found in E1-c. Figures 4c and 4d show Υ and the raw estimate for Υ_b during the forcing period. Figure 4d also shows the two variants of the analytic N^2-reduction factor Υ_b^{E1-c} [Eq. (D5)] used in L1-c1 and L1-c2.

For L3-1 and L3-2, Υ_b is modeled after the cloud coverage in E3. Here, the removal of secondary circulation from the basic state lets middle-to-upper tropospheric cloud water expand its domain during the forcing period (see appendix C). The result is a broadening of the N^2-reduction factor. Figures 4e and 4f show Υ and the raw estimate for Υ_b during the forcing period. Figure 4f also shows the two variants of the analytic N^2-reduction factor Υ_b^{E3} [Eq. (D4)] used in L3-1 and L3-2. Two variants are again considered because of uncertainty in how the simplified model should parameterize the complexities of E3, such as slantwise convection and vertical variation of moist-stability.

3.3 Two Misalignment Modes of Special Interest

In all cases considered, the linear perturbations generated by misalignment forcing are largely controlled by two discrete modes: the PTM and the inner wobble mode (IWM). The natural behavior of each mode is seen when $\hat{F}^u = \hat{F}^v = 0$. Under this force-free condition, each mode has the form $\hat{v} = V(r)e^{-i\omega t}$ and likewise for all other variables. The complex frequency $\omega \equiv \omega_R + i\omega_I$ can be found by a variety of methods. One method is to solve for the eigenfrequencies of an ordinary differential equation (in r) for the wavefunction, with radiative outer boundary conditions [cf. SM04]. If the PTM is a damped quasimode, its wave equation must be solved along a complex radial contour. An alternative method is to initialize the unforced linear system with a quasi-balanced perturbation, in which $\hat{\zeta} \propto d\bar{\zeta}/dr$, and extract ω from the time series of (say) $\hat{u}$ at a select radius. To avoid complications that might arise in defining an appropriate contour for the wave equation in searching for strongly damped quasimodes in nonmonotonic vortices, the alternative approach is used here for strongly damped PTMs (see appendix E).

Figure 5 shows the radial and azimuthal velocity wavefunctions of the PTM and the IWM of the dry vortex in L2. The structural contrast seen here is typical. The IWM is essentially confined to r less than the radius of maximum wind (RMW), whereas the PTM extends to the periphery of the vortex. Figure 6 shows the complex frequencies of the PTMs and IWMs for all versions of the linear model listed in Table 2. The IWM oscillation frequencies are invariably close to the maximum of $\bar{\Omega}$, which is greater in the contracted vortex of L1-c1, L1-c2 and L2-c. The PTM oscillation frequencies (precession speeds) are relatively slow.

In contrast to many earlier studies, the PTMs of the primary vortex (in L1-1, L1-2, L2, L3-1 and L3-2) have positive growth rates. When the vortex is completely dry, the growth rate of the PTM exceeds that of the IWM. The appreciable positive growth rate of the dry

PTM coincides with a positive value of $d\bar{\zeta}/dr$ at the critical radius $r_* = 312$ km. Note that for wavenumber-1 perturbations, the critical radius is obtained from the relation $\bar{\Omega}(r_*) = \omega_R$. As $\Upsilon_b N^2$ decreases in the eyewall region of the primary vortex, ω_R slightly increases and r_* shifts inward toward a region where $d\bar{\zeta}/dr$ is significantly smaller. The structure of the PTM also changes considerably (see below). The result is neutralization of the PTM.

The PTMs of the contracted vortex (in L1-c1, L1-c2 and L2-c) exhibit more familiar behavior. The dry PTM of L2-c is a strongly damped quasimode with negative $d\bar{\zeta}/dr$ at $r_* = 194$ km. Decreasing $\Upsilon_b N^2$ increases ω_R and reduces r_* to where the negative magnitude of $d\bar{\zeta}/dr$ is amplified. A notable caveat is the emergence of a second critical radius near the center of the vortex. Nevertheless, the end result of lowering the static stability is greater damping of the PTM.

The growth rates of the IWMs are clearly less sensitive to the variation of $\Upsilon_b N^2$ considered here. A more general study of IWM growth rate variability that considers greater reduction of N^2 in the eye, where the bulk of the IWM resides, is deferred to a later time.

Because the PTM is of principal importance to the numerical experiments under consideration, further discussion of its structure is worthwhile. Figures 7a-7c depict the dry PTM of L2.[2] Figure 7a shows snapshots of $\hat{\zeta}$ and $|\hat{\chi}|$, whereas Fig. 7b compares $\mathcal{J}^{PV}$ to $\mathcal{J}^{v\phi}$. Figure 7c shows the radial profile of the dimensionless asymmetric balance parameter, here defined for a wavenumber-1 mode by

$$\mathcal{D}^2 \equiv \frac{(\omega_R - \bar{\Omega})^2}{\mathcal{I}^2} \mathrm{sgn}(\omega_R - \bar{\Omega}), \tag{10}$$

in which $\mathcal{I}^2 \equiv \bar{\eta}\bar{\xi}$ is the inertial stability and $\mathrm{sgn}(x) = \pm 1$ for $x \gtrless 0$. In the vortex core, it is seen that $\hat{\zeta}$ is roughly proportional to $d\bar{\zeta}/dr$, $|\hat{\chi}| \ll \left|\hat{\zeta}\right|$, $\left|\mathcal{J}^{v\phi}\right| \ll \left|\mathcal{J}^{PV}\right|$, and $-1 < \mathcal{D}^2 < 0$. Approximate proportionality between $\hat{\zeta}$ and $d\bar{\zeta}/dr$ is typical of a discrete VR wave in a barotropic vortex. The condition $\left|\mathcal{J}^{v\phi}\right| \ll \left|\mathcal{J}^{PV}\right|$ is a conventional criterion for distinguish-

[2]These plots do not show the attendant perturbation in the skirt of the vortex, where the critical layer resides. While the vorticity and divergence perturbations are relatively small in the skirt, the angular pseudomomentum density is substantial in the neighborhood of r_*.

ing VR waves from inertia-gravity waves [cf. Chen et al. 2003 (C03)]. Given that $\mathcal{I}^2$ and $\bar{\Omega}$ are positive, negative $\mathcal{D}^2$ verifies the retrograde motion expected of a VR wave whose angular pseudomomentum density is peaked in a region where $d\bar{\zeta}/dr < 0$ [cf. Montgomery and Kallenbach 1997]. The condition $|\mathcal{D}^2| < 1$ implies that the intrinsic frequency of the PTM is less than the local inertial frequency. The conditions $|\mathcal{D}^2| < 1$ and $|\hat{\chi}| \ll \left|\hat{\zeta}\right|$ further suggest that the PTM obeys quasi-balanced dynamics [cf. Shapiro and Montgomery 1993; Montgomery and Lu 1997; Möller and Montgomery 2000; McWilliams et al. 2003]. In summary, the characteristics of the dry PTM are consistent with those of a quasi-balanced VR wave.

Figures 7d and 7e show that sufficient reduction of N^2 suppresses the inner part of the PTM, makes the core maximum of $|\hat{\chi}|$ comparable to that of $\left|\hat{\zeta}\right|$, and makes the core maximum of $\left|\mathcal{J}^{v\phi}\right|$ comparable to that of $\left|\mathcal{J}^{PV}\right|$. The greater amplitudes of $|\hat{\chi}|$ and $\left|\mathcal{J}^{v\phi}\right|$ may bring into question the VR wave nature of the moist PTM. On the other hand, the condition $-1 < \mathcal{D}^2 < 0$ is maintained in the vortex core (not shown). By remaining slow and retrograde, the moist PTM retains two key features of the dry VR wave from which it derives.

3.4 Response to Forcing

Figure 8a depicts the evolution of $v' = \hat{v}(r,t)\cos(\pi z/H)e^{i\varphi} + c.c$ in the dry vortex of L2 when Eqs. (6)-(8) are integrated forward in time. All perturbation fields are initially set to zero, but gain strength during the forcing interval $0 \leq t \leq \tau$. After forcing, the low frequency oscillations of the PTM dominate and continue to grow owing to intrinsic instability. It is reasonable to assume that the growth of the PTM would slow down considerably with time in a nonlinear model that accounts for mode-mode interactions and the leveling of φ-averaged PV in the vicinity of r_*.

Figures 8b and 8c illustrate how reduction of N^2 in moist versions of the same vortex inhibits the excitation of the PTM. Immediately after the forcing period, the maximum amplitudes of v' in the moist vortices of L1-2 and L3-2 are less than half the maximum found in the dry vortex. At the same instant, the average amplitudes of v' between the RMW and twice the RMW are less than 0.4 times their counterpart in the dry vortex.[3] Lesser excitability of the moist PTM seems attributable to the growth rate reduction and structural change of the mode attending the depression of N^2 in the vicinity of the eyewall. Note that despite having a smaller amplitude, the moist PTM persistently dominates v' outside the RMW for days after the forcing stops. In contrast, high frequency IWM oscillations are not discernible until very late in the v' curve corresponding to $r = 0.2$ km. The preceding result indicates weak coupling between the IWM and the applied forcing.

Figures 9a and 9b illustrate how the linear response to misalignment forcing can change with the basic state of the vortex. Specifically, these figures depict the evolution of v' in the contracted vortices of L2-c and L1-c1. To begin with, the forcing does not appear to excite the dry PTM of L2-c as strongly as the dry PTM of L2. Once the forcing stops, the maximum amplitude of v' in L2-c is just 0.4 times the corresponding maximum in L2. It seems reasonable to assume that the PTM of L2-c is less responsive partly because of its rapid intrinsic damping. Such damping is evident in the quick decay of the post-forcing oscillations in v' that occur with the natural PTM period outside the RMW. With moisture added to the system in L1-c1, the freed PTM existing for $t > \tau$ is practically negligible. With or without moisture, fast IWM oscillations eventually dominate v' over the entire vortex. In a more realistic model, nonlinear saturation could very well prevent the IWM from dominating the perturbation outside the RMW.

4. Response to Misalignment Forcing in the Cloud Model

The following evaluates the predictions and assumptions of the SLT by comparison to the CM experiments. The evaluation begins by demonstrating the qualitatively correct prediction

[3]Comparable amplitude reductions are found in the radial velocity perturbation u'.

that moisture inhibits misalignment. It then proceeds to a more detailed and quantitative assessment of the predicted dry and moist tilt dynamics.

4.1 Development of Misalignment and Vertical Antisymmetry in the Main CM Experiments

The CM experiments are first compared to one another using the following direct measure of vertical misalignment:

$$M \equiv \sqrt{\int_{z_s}^{z_t} \frac{dz}{z_t - z_s} |\mathbf{x}_c - \mathbf{x}_{ca}|^2} \Bigg/ \int_{z_s}^{z_t} \frac{dz}{z_t - z_s} r_{max}, \tag{11}$$

in which $\mathbf{x}_c \equiv (x_c, y_c)$ is the horizontal position vector of the rotational center at height z, and $\mathbf{x}_{ca}$ is the z-average of $\mathbf{x}_c$ between $z_s = 30$ m and $z_t = 10.7$ km. The values of the Cartesian coordinates x_c and y_c specifically correspond to the center of the polar coordinate system that maximizes the peak value of the φ-averaged azimuthal velocity $\bar{v}$ at fixed z. The height-dependent radius of maximum $\bar{v}$ is denoted r_{max} and appears in the denominator of M. In words, M is the root-mean-square displacement of rotational centers from their vertical mean, normalized to the vertical mean of r_{max}.

Figure 10a shows M versus time for the four main CM experiments E1-E4. Consistent with the SLT, the moist convective vortex in E1 is substantially less responsive to the applied misalignment forcing than the dry nonconvective vortex in E2. The forcing also has trouble perturbing the non-precipitating cloudy vortex in E3, suggesting that reduction of static stability may be sufficient to prevent substantial tilt. Whether or not this mechanism strongly inhibits tilt in E1 is uncertain at this point, partly because differences emerge in the N^2-reduction profiles of E1 and E3 during the forcing period [Fig. 4]. Furthermore, E4 shows that M is considerably reduced in a dry vortex with a thermally driven SSC. It stands to reason that the presence of the SSC could help limit tilt in the E1-hurricane.

The supplemental notes in appendix C address the basic premises used to infer from the results of E3 and E4 that both static stability reduction by cloud coverage and the SSC may introduce viable mechanisms for inhibiting tilt. Appendix C.1 presents evidence that the cloudy vortex in E3 does not develop an appreciable SSC, and that its wavenumber-1 thermodynamics is consistent with substantial diabatic reduction of static stability. Appendix C.2 verifies that the SSC in E4 is comparable to that in E1, and that the wavenumber-1 thermodynamics in E4 is quasi adiabatic.

Note that small departures from equilibrium at $t = 0$ and weak instabilities cause M to grow somewhat without applied forcing. The discrete symbols in Fig. 10a show the unforced growth of M during the time interval $0 \leq t \leq \tau$. The data were obtained by letting $A \rightarrow 0$ in Eq. (5) and repeating experiments E1-E4. The unforced version of E1 is denoted E1×0 and likewise for E2-E4. It is verified that the initial forced growth of M substantially exceeds that found in each unforced experiment.

The tendency equation of an alternative variable connected to misalignment will be examined in section 4.4 to help assess the influence of the SSC in E1. This variable is called the vertical antisymmetry parameter (VAP) and is defined by

$$\begin{aligned} \mathrm{VAP}^2 &\equiv \frac{1}{2\pi(r_o^2 - r_i^2)(z_t - z_b)^2} \int_{r_i}^{r_o} r dr \int_0^{2\pi} d\varphi \left[\int_{z_b}^{z_t} dz (v_1 e^{i\varphi} + c.c.) G \right]^2 \\ &= \left\langle \left| \langle v_1 \rangle_z \right|^2 \right\rangle_r . \end{aligned} \tag{12}$$

Here, $v_1(r, z, t)$ is the complex wavenumber-1 Fourier component of v, defined in the cylindrical coordinate system centered at $\mathbf{x}_{ca}(t)$. The weight function $G(z) \equiv (2z - z_t - z_b)/(z_t - z_b)$ is antisymmetric about the mean height (z_m) in the integral over z, and has values of ± 1 at the two end-points. The notation $\langle h \rangle_z$ represents $\int_{z_b}^{z_t} dz h G/(z_t - z_b)$, whereas $\langle h \rangle_r$ represents $2 \int_{r_i}^{r_o} r dr h/(r_o^2 - r_i^2)$. The limits of integration are chosen to be $r_i = 65$ km, $r_o = 165$ km, $z_b = 2.1$ km and $z_t = 10.7$ km. The integration volume therefore covers the bulk of the eyewall updraft in E1.

Figure 10b shows that VAP behaves much like M in the CM experiments under consideration. However, the two quantities are distinct. For example, VAP includes contributions from antisymmetric components of v_1 that are not directly attributable to misaligned centers of rotation. One such component is the weak ambient vertical wind-shear superposed on the vortex flow during the forcing period. VAP also gives less weight to misalignments that have small vertical wavelengths, and no weight to misalignments in which v_1 is symmetric about z_m. Note that because VAP has no contribution from the vertically invariant component of v_1, it does not depend on the velocity of the reference frame.

4.2 Detailed Response of the Dry Nonconvective Vortex in E2

The SLT of section 3 showed that a PTM dominates the tilt generated by slow misalignment forcing in the dry barotropic analogue of the simulated hurricane. It is here verified that the same is true in the dry baroclinic analogue.

Figure 11 displays snapshots of the z-dependent rotational centers $\{(x_c, y_c)\}$ of the baroclinic vortex in E2. All snapshots are taken after the forcing period, in a coordinate system centered at $\mathbf{x}_{ca}(t)$. To within a fair approximation, the displacement of (x_c, y_c) from the lowest center of rotation increases unidirectionally with height, indicating a clean tilt. The tilt precesses with an angular frequency of $\omega_R = 6.8 \times 10^{-5}$ s^{-1}. The corresponding 26-h rotation period is merely 13% less than that of the dry PTM of the barotropic vortex of L2.

Figures 12a-12c illustrate the basic structural similarity of the tilt mode in E2 with the corresponding PTM of the SLT [Figs. 7a-7c]. The plotted fields are defined using an isentropic cylindrical coordinate system centered at $\mathbf{x}_{ca}$. The definitions involve the wavenumber-1 and wavenumber-0 components of the following Fourier expansion: $v \equiv \sum_{l=-\infty}^{\infty} v_l(r, \theta, t) e^{il\varphi}$ and likewise for all other fields. The definitions also involve the time average $\langle \ldots \rangle_T$ over the free evolution period $\tau \leq t \leq \tau + T$, in which $T \approx 2$ d.

Figure 12a is a contour plot of the asymmetric balance parameter,

$$\mathcal{D}_\theta^2 \equiv \frac{(\omega_R - \bar{\Omega})^2}{\mathcal{I}_\theta^2}\mathrm{sgn}(\omega_R - \bar{\Omega}), \quad (13)$$

in which $\bar{\Omega} \equiv \langle v_0 \rangle_T / r$ and $\mathcal{I}_\theta^2 \equiv [\partial_r(r \langle v_0 \rangle_T)/r + f](2\bar{\Omega} + f)$. The preceding definition of $\mathcal{D}_\theta^2$ is the analogue of $\mathcal{D}^2$ [Eq. (10)] for dry baroclinic vortices [cf. Shapiro and Montgomery 1993]. Figure 12b shows superposed contour plots of the wavenumber-1 isentropic vorticity amplitude $\langle |\zeta_{\theta,1}| \rangle_T$ and divergence amplitude $\langle |\chi_{\theta,1}| \rangle_T$. As usual, $\zeta_\theta \equiv [\partial_r(rv) - \partial_\varphi u]/r$ and $\chi_\theta \equiv [\partial_r(ru) + \partial_\varphi v]/r$. Note that the partial derivatives appearing in the definitions of $\mathcal{I}_\theta^2$, ζ_θ and χ_θ are evaluated at constant θ. Figure 12c essentially shows superposed contour plots of the two components of the isentropic angular pseudomomentum density $\mathcal{J}_\theta$ associated with the $l = 1$ disturbance [cf. C03; Schecter 2008 (S08)]. More precisely, the plotted quantities are

$$\mathcal{J}_\theta^{PV} \equiv -\left\langle \frac{r\,(\overline{\sigma}^s)^2\,|\mathrm{PV}_{\theta,1}|^2}{2\,\partial_r \overline{\mathrm{PV}}_\theta^s} \right\rangle_T \quad \text{and} \quad \mathcal{J}_\theta^{v\sigma} \equiv -\left\langle \Re\left[r v_1 \sigma_1^*\right] \right\rangle_T, \quad (14)$$

in which $\overline{\sigma}^s$ equals $\langle \sigma_0 \rangle_T$ and $\overline{\mathrm{PV}}_\theta^s$ equals $\langle \mathrm{PV}_{\theta,0} \rangle_T$ smoothed with 10 km radial boxcar averaging. The isentropic density σ and potential vorticity PV_θ were defined in section 2.2. For dry baroclinic vortices, comparing $\mathcal{J}_\theta^{PV}$ to $\mathcal{J}_\theta^{v\sigma}$ is analogous to comparing $\mathcal{J}^{PV}$ to $\mathcal{J}^{v\phi}$ in the simple linear model of section 3. Like the PTM of the SLT, it is seen that the core perturbation has the following retrograde VR wave characteristics: $-1 < \mathcal{D}_\theta^2 < 0$, $|\chi_{\theta,1}| \ll |\zeta_{\theta,1}|$, and $|\mathcal{J}_\theta^{v\sigma}| \ll \left|\mathcal{J}_\theta^{PV}\right|$. Here, the order-of-magnitude relations pertain to peak values.

Figures 12d and 12e show r-t Hovmöller diagrams of $\Re[\mathrm{PV}_{\theta,1}(r,\theta,t)]$ during the free evolution period, at $\theta = 298.7$ and 331.4 K (the bold θ contours in Fig. 12a). The primary 26-h oscillations are approximately 180^o out of phase in the upper and lower troposphere, and are attributable to the slow PTM. Faster secondary oscillations are found in the lower-tropospheric portion of the inner core. Their frequency seems to exceed that of the deep misalignment IWM considered in linear response theory. Such minor fluctuations are noticeable partly because the PTM fails to grow to the extent seen in the SLT. To accurately predict the saturation amplitude of the PTM would require a nonlinear theory that incorporates the evolution of basic-state PV, especially in the neighborhood of the critical radius [cf. Balmforth et al. 2001 (B01); Schecter and Montgomery 2006 (SM06); S08]. A nonlinear theory would also help predict changes in the radial waveform of the PTM tied to changes in the radial gradient of basic-state PV that seem to have taken place in the vortex core mostly during the forcing period [Fig. 12f].

4.3 Detailed Response of the Moist Convective Vortex in E1

Figure 13 compares the moist tilt dynamics of E1 to that predicted by the SLT. The SLT is specified as in L1-2, where the PTM is effectively neutral. The alternative L1-1 specification is ruled out of consideration, because there is no clear evidence in E1 of its relatively fast growing PTM.

Figures 13a and 13b show the amplitude and orientation angle of tilt vectors in E1 and the SLT during and after the forcing period. The tilt vector is here defined by

$$\delta\mathbf{x}_c \equiv \mathbf{x}_c(z_2) - \mathbf{x}_c(z_1), \tag{15}$$

in which $z_2 = 9$ km. The value of z_1 is somewhat arbitrary given the approximate invariance of $\mathbf{x}_c$ in the lowest 2 km of E1, but is here set to 30 m. An orientation angle of zero corresponds to an eastward tilt. As explained in section 4.1, $\mathbf{x}_c$ is determined by the velocity field in the vicinity of r_{max}, which is on the outer edge of the eyewall updraft in E1. In this sense, the present definition of tilt marginally pertains to misalignment of the outer core.[4] Note that the velocity field used to obtain $\mathbf{x}_c$ and tilt in the SLT is given by the initial basic-state plus the wavenumber-1 perturbation; second order changes to the flow are

[4] Circumstances may exist in which $\delta\mathbf{x}_c$ is not firmly tied to vertical misalignment in the very outer core. Such misalignment is of interest for how it may contribute to the enhancement of low entropy downdrafts that could limit TC intensity [Riemer et al. 2010,2013; Tang and Emanuel 2010].

unaccounted for.[5] Barring greater fluctuations and somewhat greater decay after the forcing period, the tilt vector of E1 evolves much like its counterpart in the SLT.

Figures 13c-13f show the wavenumber-1 component of midlevel vertical velocity w^{md}. By definition,

$$w^{md}(\varphi, t) \equiv \frac{1}{(r_d - r_c)(z_d - z_c)} \int_{z_c}^{z_d} dz \int_{r_c}^{r_d} dr w, \tag{16}$$

in which $z_c = 5.0$ km, $z_d = 7.1$ km, and the radial limits of integration are adjustable. The polar coordinate system in E1 is centered at $\mathbf{x}_{ca}$, which meanders and ends up roughly 70 km from where it began. The azimuthal Fourier expansion of w^{md} is written $w^{md} \equiv \sum_{l=-\infty}^{\infty} w_l^{md}(t) e^{il\varphi}$. The total wavenumber-1 component is defined by $W_1^{md} = w_1^{md}(t)e^{i\varphi} + c.c.$ The crest amplitude of W_1^{md} is $2|w_1^{md}|$ and the crest azimuth is $\varphi = -\arg(w_1^{md})$.

Figures 13c and 13d show time series of the crest amplitude and azimuth of W_1^{md} in the outer core, computed with $r_c = 120$ km and $r_d = 200$ km. Here there is fairly good agreement between E1 and the SLT.[6] Note that in both cases, the crest azimuth of W_1^{md} lags behind the tilt angle.

Figures 13e and 13f show time series of the crest amplitude and azimuth of W_1^{md} in a region that includes the eyewall, bounded by $r_c = 70$ km and $r_d = 150$ km. Figure 13f also shows the wavenumber-1 crest azimuths of the midlevel heating rate $(D\theta/Dt)$ and column integrated rain-mass density in the same radial segment of the E1-hurricane. It is seen that the crest azimuths of the vertical velocity, heating rate and rain-mass waves approximately coincide. Such a result is agreeable with the moisture parameterization of the SLT, but there is also cause for concern. Specifically, W_1^{md} in E1 is generally out of phase with its counterpart in the SLT. The crest azimuth lags behind the tilt angle in the SLT, but roughly

[5] The reliability of measuring tilt with a linearized perturbation was tested by horizontally displacing each layer of the unperturbed circular vortex of the SLT by an amount $\boldsymbol{\epsilon}(z)$ and approximating the new velocity field only to first order in $|\boldsymbol{\epsilon}|$. The tilt vector $\delta\mathbf{x}_c$ obtained from the approximate velocity field was in good agreement with the displacement vector $\boldsymbol{\epsilon}(z_2) - \boldsymbol{\epsilon}(z_1)$ for amplitudes not exceeding about 25 km. Although the amplitude error grew with increasing displacement, the orientations of the tilt vector and displacement vector persistently agreed.

[6] Similar agreement was found when considering W_1^{md} in an arbitrary subregion of the outer core, bounded by $r_c = 140$ km and $r_d = 160$ km.

equals the tilt angle in E1. The crest azimuth in E1 also deviates considerably from its linear trend in time once the forcing stops.

In summary, the SLT appears to predict tilt and midlevel convection in the outer core better than perturbations to convection in the eyewall. There is no obvious reason why inner core discrepancies should not corrupt outer core dynamics in E1. However, quasi-independent outer core dynamics seems plausible if the bulk of the PTM is outside the eyewall updraft. This scenario is somewhat suggested by the SLT [Figs. 7d and 7e].

4.4 VAP^2 Growth Rate Analysis

Section 4.3 suggested that the SLT cannot fully explain how the eyewall region of the hurricane responds to weak misalignment forcing. The eyewall region contributes substantially to the wavenumber-1 vertical antisymmetry parameter VAP [Eq. (12)]. Evaluation of the factors controlling the growth rate of VAP^2 may therefore help one identify significant elements of eyewall dynamics neglected by the SLT. The following analysis makes use of the Fourier expansion $v \equiv \sum_{l=-\infty}^{\infty} v_l(r, z, t)e^{il\varphi}$ and likewise for all other fields.

The tendency equation for VAP^2 is obtained directly from the $l = 1$ component of the azimuthal velocity equation and is conveniently written

$$d(\mathrm{VAP}^2)/dt = S_i^0 + S_i^1 + S_e, \tag{17}$$

in which the subscript i/e denotes a source that is intrinsic/extrinsic to the moist primitive-equation dynamics of the system. The first intrinsic source on the rhs of Eq. (17) has a direct analogue in the SLT. It is given by $S_i^0 \equiv S_{amg} + S_{pg}$, in which

$$\begin{aligned} S_{amg} &\equiv -2 \left\langle \Re \left[\langle v_1 \rangle_z^* \langle u_1\eta_0 + w_1\partial_z v_0 \rangle_z \right] \right\rangle_r \quad \text{and} \\ S_{pg} &\equiv 2 \left\langle \Im \left[\langle v_1 \rangle_z^* \langle \theta_{vr}\Pi_1/r \rangle_z \right] \right\rangle_r . \end{aligned} \tag{18}$$

The term S_{amg} is connected to the *angular momentum gradient* of the symmetric flow. Specifically, S_{amg} derives from the following term in the v_1-tendency equation: $-u_1\partial_r(\mathcal{L}_0)/r - w_1\partial_z\mathcal{L}_0/r$, in which $\mathcal{L}_0 \equiv rv_0 + fr^2/2$ is the angular momentum. Note that $\partial_r(\mathcal{L}_0)/r \equiv \eta_0$. The term S_{pg} is associated with the *pressure gradient* force. As in many CMs, the explicit pressure-gradient term $\theta_v\partial_\varphi\Pi/r$ in the v-equation is here approximated by $\theta_{vr}\partial_\varphi\Pi/r$, in which θ_v and θ_{vr} are the actual and reference-state virtual potential temperature distributions. The operator $\Im[\ldots]$ in Eq. (18) denotes the imaginary part of the quantity in square brackets.

The second intrinsic source on the rhs of Eq. (17) has no direct analogue in the SLT. It is given by $S_i^1 \equiv S_{ssc} + S_{svs} + S_{ww} + S_{trb}$, in which

$$\begin{aligned} S_{ssc} &\equiv -2\left\langle \Re\left[\langle v_1\rangle_z^* \left\langle u_0\partial_r\left(rv_1\right)/r + w_0\partial_z v_1\right\rangle_z\right]\right\rangle_r, \\ S_{svs} &\equiv 2\left\langle \Im\left[\langle v_1\rangle_z^* \left\langle v_1 v_0\right\rangle_z/r\right]\right\rangle_r, \\ S_{ww} &\equiv -2\left\langle \Re\left[\langle v_1\rangle_z^* \left\langle \sum_{m\neq 0,1}\frac{u_m}{r}\partial_r(rv_{1-m}) + i(1-m)\frac{v_m v_{1-m}}{r} + w_m\partial_z v_{1-m}\right\rangle_z\right]\right\rangle_r, \end{aligned} \tag{19}$$

and S_{trb} will be defined shortly. The term S_{ssc} is connected to the *symmetric secondary circulation*. The term S_{svs} is connected to the *symmetric vertical* wind-*shear*, since it would be zero if v_0 were independent of z. The term S_{ww} accounts for nonlinear, asymmetric *wave-wave* interactions. The term S_{trb} is associated with subgrid *turbulent* transport; it is expressed here by $S_{trb} \equiv 2\left\langle \Re\left[\langle v_1\rangle_z^* \langle D_{v,1}\rangle_z\right]\right\rangle_r$, in which $D_{v,1}$ is the wavenumber-1 component of the tendency term connected to "eddy-viscosity" in the azimuthal velocity equation. The extrinsic source in Eq. (17) is simply

$$S_e \equiv 2\left\langle \Re\left[\langle v_1\rangle_z^* \left\langle(\hat{\boldsymbol{\varphi}}\cdot\dot{\mathbf{v}}_a)_1\right\rangle_z\right]\right\rangle_r, \tag{20}$$

in which $\dot{\mathbf{v}}_a$ is given by Eq. (5).

The instantaneous growth rate of VAP^2 may be written $d\ln(\mathrm{VAP}^2)/dt = \sum_\alpha \tilde{S}_\alpha \equiv \tilde{S}_{tot}$, in which the individual source terms are related to those of $d(\mathrm{VAP}^2)/dt$ by $\tilde{S}_\alpha \equiv S_\alpha/\mathrm{VAP}^2$.

Figures 14a and 14b show $\tilde{S}_{tot}$ and its components during the first 12 h of E1 and E2, in a reference frame moving with and centered at $\mathbf{x}_{ca}$. The initial VAP^2 growth rates are directly controlled by the applied misalignment forcing ($\tilde{S}_e$), but other factors shortly weigh in. In E1, the influence of $\tilde{S}_i^1$ on the vertical antisymmetry of the moist convective vortex is comparable and essentially opposite to that of $\tilde{S}_i^0$. Moreover, the value of $\tilde{S}_i^1$ is largely determined by the SSC component, which first hinders and then promotes the growth of VAP^2. The magnitudes of $\tilde{S}_{svs}$ and $\tilde{S}_{ww}$ do not exceed 1.8×10^{-4} s^{-1}, and $\tilde{S}_{trb}$ is subdominant to both (not shown). The dry nonconvective vortex of E2 exhibits simpler dynamics, in that $\tilde{S}_i^1$ has only a minor (and mostly negative) influence on the growth of VAP^2 through $\tilde{S}_{svs}$.

The VAP^2 growth rate analysis for E1 suggests that an accurate theory for how the inner core of a mature hurricane responds to weak misalignment forcing may need to incorporate the SSC. Further inferences would be more speculative. The analysis does not overtly reveal the primary mechanism by which the SSC influences VAP^2, let alone direct measures of misalignment. Like reduced static stability, the SSC could independently alter the structure of the PTM and thereby affect source terms other than $\tilde{S}_{ssc}$. Another caveat worth noting is that the $l = 0$ and $l = 1$ modes commingle to a degree when the coordinate center is varied. A shift of $\mathbf{x}_{ca}$ at an arbitrary time t could alter source terms such as $\tilde{S}_{amg}$ and $\tilde{S}_{ssc}$ in opposite directions. That said, the results in Fig. 14 do not change qualitatively when the coordinate center is fixed at its original ($t = 0$) location.

4.5 Response of the Contracted Vortex

The SLT of section 3 predicted that the contracted vortices of E1-c and E2-c would have faster and less excitable PTMs than their counterparts in E1 and E2. This prediction seems qualitatively consistent with the CM experiments.

Figure 15 displays time series of the tilt vector components after the forcing periods in E1, E2, E1-c and E2-c. Thick curves show data smoothed with 5-h boxcar averaging to highlight oscillations in the PTM frequency range. PTM signals are clearly evident in the tilt vectors of the dry vortices of E2 and E2-c. The 13.7-h oscillation period of the PTM in E2-c is 19% greater than predicted by the corresponding SLT, but is still substantially less than its counterpart in E2. Nonlinear processes in E2-c prevent the continual damping of the PTM found in the SLT, but the prediction of reduced excitability relative to E2 holds.[7] Unlike the tilt vector of E2, the tilt vector of E2-c has a prominent secondary oscillation whose 3-h period equals that of an IWM. The appearance of this signal seems agreeable with the SLT [Fig. 9a].

Although the tilt vector of the moist convective hurricane in E1 exhibits weak oscillations at the expected PTM frequency, the contracted hurricane of E1-c shows no discernible sign of a PTM. The latter result is consistent in principle with very strong PTM damping found in the SLT of the contracted vortex with moisture parameterized as in L1-c1 or L1-c2.

4.6 Comment on Eyewall Convection in E1 and E1-c

It is worth remarking that with $A = 1$ m s^{-1} chosen for the forcing function, the precipitation rings defining the eyewalls of the hurricanes in E1 and E1-c do not severely break down. Figure 16a shows how the ring of column integrated rain mass in E1 is maintained throughout the simulation. Ring maintenance suggests that the wavenumber-1 component of w is insufficiently strong in the eyewall to create a broad region of unsaturated downdraft. For comparison, Fig. 16b shows substantial desymmetrization of the ring in a similar experiment (E1×4) with $A = 4$ m s^{-1}. On the one hand, the SLT might be more appropriate for cases in which perturbation-w is relatively strong compared to the SSC. On the other hand, the fundamental assumption of linear dynamics (made in the SLT) seems more problematic for cases in which the perturbation is large and cloudy only on its updraft side [cf. Patra

[7]Like the dimensional magnitude of the tilt vector, the nondimensional misalignment M is also reduced. The mean value of M during the free evolution period in E2-c is approximately 44% of the corresponding mean in E2.

2004]. A detailed comparison of the SLT to the behavior of large amplitude tilts in mature hurricanes is deferred to a future time.

4.7 Comment on Subgrid Turbulent Transport in the CM Experiments

As noted earlier, the mixing coefficients in the CM experiments were adjusted to minimize the impact of turbulent transport on tilt dynamics without creating excessive noise. On the fine grid, the horizontal mixing coefficient for momentum K_h had an approximately constant value of 593 $\mathrm{m^2s^{-1}}$ in all simulations. The vertical mixing coefficient for momentum K_v was determined by a Smagorinsky-type closure and varied in each numerical experiment. Figure 17 shows the azimuthally averaged values of K_v output by the CM during the forcing periods of E1-E4. It is seen that K_v is of order unity or less in the middle troposphere.

The time scales for turbulent transport in the horizontal and vertical directions are reasonably estimated by $\tau_h \equiv \lambda_h^2/K_h$ and $\tau_v \equiv \lambda_v^2/K_v$, in which λ_h and λ_v are the horizontal and vertical lengthscales of the structure of interest. For $\lambda_h = 10$ and 100 km, $\tau_h = 47$ and 4.7×10^3 h. For $\lambda_v = 4$ km and $K_v =$ 1-10 $\mathrm{m^2s^{-1}}$, $\tau_v = 4.4 \times 10^3$-10^2 h. Using the scalar mixing coefficients would reduce each of the previous time scale estimates by a factor of 3. The short estimate of τ_h for λ_h=10 km suggests that parameterized turbulence may have caused modest radial smoothing of basic-state PV over the course of each simulation. However, the large estimates of τ_v and of τ_h with λ_h=100 km provide some reassurance that parameterized turbulence had little direct influence on the simulated vortex-scale tilts.

5. Concluding Remarks

This paper compared the tilt dynamics of a simulated hurricane to the predictions of a simple linear theory (SLT) that neglects the symmetric secondary circulation (SSC) and treats moisture merely as a local reduction of static stability (N^2). The primary hurricane simulation (E1) was carried out with a traditionally configured CM. Additional simulations were conducted with reduced physics and/or modified vortex structure to help identify features that enable the hurricane to resist tilting when exposed to misalignment forcing. The main results are summarized and discussed below.

The simplest CM experiment (E2) consisted of a dry nonconvective vortex closely resembling the primary hurricane. The vortex was subjected to a period of idealized misalignment forcing and then left to freely evolve with time. As predicted by the SLT, the forcing primarily excited a slowly precessing tilt mode (the PTM) with VR wave characteristics.

Also as predicted, the same misalignment forcing generated much weaker tilt in the primary hurricane experiment. According to the SLT, lesser tilt was caused by moisture-induced reduction of N^2 in the vicinity of the eyewall. Such reduction of N^2 theoretically limited the excitability of the PTM by neutralizing its growth rate and altering its structure, while just slightly changing its natural precession frequency. An additional CM experiment (E3) with suspended cloud water but seemingly negligible SSC supported the SLT result that reduction of N^2 is sufficient to inhibit the excitation of a PTM.

In a more detailed comparison to theory, the tilt vector [Eq. (15)] in the primary hurricane experiment was found to vary with time much like its counterpart in the SLT. However, the theoretical phase relation between the tilt angle and the crest azimuth of the attendant midlevel vertical velocity wave seemed to hold only in the outer core of the simulated hurricane. The inner core discrepancy suggested some deficiencies in how the SLT parameterizes perturbations to diabatic convection in the vicinity of the eyewall. It is not entirely clear how to reconcile these deficiencies with the successful prediction of tilt evolution. On the other hand, neglected eyewall processes are conceivably incidental if the bulk of the PTM resides in the outer core [cf. Figs. 7d and 7e].

The qualified success of the SLT was further challenged by a final CM experiment (E4) that excluded moisture but kept the SSC through an artificially distributed heat source. The reduced misalignment found in E4 supported the intuitive notion that the SSC may independently inhibit tilt. Fully understanding the mechanism will require further investigation. One might speculate that the presence of the SSC changes the complex frequency and structure of the PTM in such a way that renders it less excitable. This hypothetical mechanism for limiting the growth of outer tilt would be analogous to that which occurs by reducing N^2 in the SLT. A more straightforward effect of the SSC on tilt dynamics was examined in the eyewall region of the E1-hurricane. Convective transport by the SSC seemed to oppose the growth of wavenumber-1 vertical antisymmetry (VAP) in the eyewall during the early stage of forcing, but its negative influence did not persist.

Note that the structure of the primary hurricane considered in this study was well suited to illustrate the potential importance of the PTM in governing tilt and the potential importance of moist convection in limiting tilt. As predicted by the SLT, a slightly stronger and contracted vortex was found to have a less dominant PTM that effectively resisted excitation even without moisture.

In brief summary, the SLT offers partially valid insight on how tilt develops in hurricanes exposed to misalignment forcing. A more advanced theory that properly incorporates the SSC (and the boundary layer) seems needed to clarify some unresolved issues on how moist convection in the eyewall affects tilt dynamics.

Acknowledgments: The author thanks Dr. Paul Reasor for several discussions that helped motivate parts of this paper. The author also thanks Dr. Chun-Chieh Wu and two anonymous reviewers for their constructive comments on the original manuscript that led to several improvements. This work was supported by NSF grants AGS-1101713 and AGS-1250533. Most of the numerical simulations were performed on NCAR/CISL supercomputers through project UNWR0001. Some preliminary numerical simulations were also carried out with SDSC resources through XSEDE project TG-ATM130028.

Appendices

A. Undamped and Growing PTMs

In linear theory, the damping rate of a PTM is basically proportional to the negative radial gradient of PV in the critical layer. If the amplitude of the PTM exceeds a modest threshold, its stirring of the critical layer will flatten the local PV distribution before significant damping occurs [cf. Briggs et al. 1970; Schecter et al. 2000; B01; SM06]. Moreover, a positive radial PV gradient in the critical layer would cause the PTM to initially grow [S02; SM03; SM04]. Transient growth may also occur through interaction of the PTM with a pre-existing disturbance [cf. Antkowiak and Brancher 2004; Nolan and Farrell 1999; Lansky et al. 1997]. Finally, PTMs in extremely intense vortices with negligible skirts of outer PV can amplify with an e-folding time of 5-10 core rotation periods by emitting spiral inertia-gravity waves with negative angular pseudomomentum [SM03; SM04; S08; cf. Hodyss and Nolan 2008; Billant and LeDizès 2009].

B. Additional Information on the Initial Setup of E1

The preliminary simulation used to obtain the initial conditions of E1 had several stages. The first stage lasted approximately 9 days with the sea-surface temperature (SST) set equal to 25 ^{o}C. During this time, the TC developed an outer eyewall that caused the demise of its inner predecessor. The model was then reinitialized with a symmetrized version of the reconfigured and relatively large convective vortex. The SST was lowered to 23 ^{o}C and the system was allowed to relax for approximately two more days. Another two days of adjustment with weaker diffusivity (achieved by the subgrid turbulence modification described in section 2.1) produced the initial condition of E1. The lower SST was used in E1 as a precaution against another eyewall replacement event.

Figure A1 compares the initial vertical distributions of actual and saturated pseudoequivalent potential temperature in E1 to those of the JMS. Both variables are approximated as in Bryan 2008 and horizontally averaged over the entire computational domain. By the end of the preliminary simulation, which did not conserve moist air mass, the domain averaged surface pressure was unnaturally high ($p_s = 1065$ hPA) and a minor temperature inversion had developed just above $z = 2$ km. While such imperfections reflected in Fig. A1 may be inadequate for modeling a real hurricane, they are not critically problematic for the purpose of this idealized study.

C. Supplemental Notes on the Reduced Physics Experiments E3 and E4

C.1 The Non-Precipitating Cloudy Vortex Experiment E3

Figure A2a illustrates the evolution of q_c in the non-precipitating cloudy vortex experiment E3. The distribution of cloud water initially resembles that of the primary hurricane in E1, but broadens over time in the middle and upper troposphere. Such broadening accounts for the distinct Υ distribution in Fig. 4e. Note that the low cloud band in the inner core is attributable to an aesthetic shortcoming of the initialization algorithm for E3. It is not thought to have a significant consequence on tilt dynamics.

Supporting evidence that cloud coverage in E3 acts to substantially reduce the effective static stability relevant to tilt dynamics is provided below. The analysis is carried out in a reference frame centered at $\mathbf{x}_{ca}$. The notation $h^{md}(\varphi, t)$ is used to represent a generic midlevel field-variable analogous to w^{md} [Eq. (16)] with $z_c = 5.0$ km, $z_d = 7.1$ km, $r_c = 70$ km and $r_d = 150$ km. As usual, one may write $h^{md} \equiv \sum_{l=-\infty}^{\infty} h_l^{md}(t) e^{il\varphi}$.

The wavenumber-1 component of midlevel potential temperature evolves according to

$$\frac{d}{dt}\theta_1^{md} = -\left(u\partial_r\theta + \frac{v}{r}\partial_\varphi\theta\right)_1^{md} - \left[1 - \frac{\dot{\Theta}_1^{md}}{(w\partial_z\theta)_1^{md}}\right](w\partial_z\theta)_1^{md}. \qquad \text{(C1)}$$

The heating rate $\dot{\Theta}$ is obtained here by computing the material derivative of θ from standard model output fields. It is found that $\dot{\Theta}_1^{md}$ and $(w\partial_z\theta)_1^{md}$ are almost exactly in phase in E3. Perfect phase agreement would allow the substitution

$$1 - \frac{\dot{\Theta}_1^{md}}{(w\partial_z\theta)_1^{md}} \;\rightarrow\; 1 - \frac{\left|\dot{\Theta}_1^{md}\right|}{\left|(w\partial_z\theta)_1^{md}\right|} \equiv \Upsilon_* \tag{C2}$$

in Eq. (C1). The dimensionless variable Υ_* therefore somewhat resembles the static stability reduction factor Υ_b in Eq. (7) of section 3. The resemblance improves to a degree as the SSC becomes negligible and the lowest order approximation of $w\partial_z\theta$ becomes $w\partial_z\theta_0$, in which θ_0 is the azimuthal mean of θ. The value of Υ_* clearly decreases from unity as $|\dot{\Theta}_1^{md}|$ increases from its dry-adiabatic value of zero. For small perturbations in the non-precipitating cloudy vortex of E3, the condition $\Upsilon_* \ll 1$ is taken to suggest that condensation and evaporation are substantially reducing the cooling and warming that would otherwise occur adiabatically in the updrafts and downdrafts of the wavenumber-1 disturbance [cf. Fig. A2b]. For other vortices in which $\dot{\Theta}_1^{md}$ and w_1^{md} are in phase but the mean updraft is more considerable, values of Υ_* less than unity might simply indicate an acceleration/deceleration of condensational heating in the positive/negative regions of the wavenumber-1 vertical velocity perturbation.

Figure A2c shows the time series of Υ_* obtained from hourly sampling of E3. The mean value of the time series is 0.11 and the standard deviation is 0.08. It has been verified that the mean of Υ_* computed with hourly output is within 5% of the mean computed with 5-min output over the intervals $1 \leq t \leq 12$ h and $24 \leq t \leq 30$ h. High frequency (5-min) output was not archived over any other intervals. Note that redefining Υ_* with the substitution $(w\partial_z\theta)_1^{md} \rightarrow \int_{z_c}^{z_d} dz \int_{r_c}^{r_d} dr w_1 \partial_z\theta_0/(r_d - r_c)(z_d - z_c)$ in Eq. (C2) changes its value by only a modest amount to 0.15 ± 0.08. The two variables on opposite sides of the substitution arrow have nearly indistinguishable phases, and their amplitudes differ by only 5% on average.

Needless to say, the SSC of the non-precipitating cloudy vortex in E3 is precisely zero only at the beginning of the experiment. The SSC is defined by the wind vector (u_0, w_0), in which u_0 and w_0 are the azimuthally averaged radial and vertical velocity fields. The following statistics of the SSC are average values obtained from hourly snapshots taken for $t \leq 35$ h. In the cylindrical shell of the E3-vortex defined by $65 \leq r \leq 165$ km and $2.1 \leq z \leq 10.7$ km, the root-mean-square (rms) radial and vertical velocities are respectively $u_0^{rms} = 0.7$ m s^{-1} and $w_0^{rms} = 0.08$ m s^{-1}. The corresponding rms velocities in the E1-hurricane are $u_0^{rms} = 5.4$ m s^{-1} and $w_0^{rms} = 0.7$ m s^{-1}. Furthermore, the shell-averages of u_0 and w_0 in E3 are merely 0.006 and 0.01 times their counterparts in E1. The minuscule means in E3 are due to lesser wind speeds (evident in the rms measurements) and greater cancellations between positive and negative velocities.

In summary, the condition $\Upsilon_* \ll 1$ in E3 seems to suggest that a substantial reduction of static stability is in effect. On the other hand, the SSC in E3 appears to be at least an order of magnitude weaker than its E1 counterpart.

C.2 The Dry Thermally Forced Vortex Experiment E4

In a fixed cylindrical coordinate system whose central axis is coaligned with that of the axisymmetric thermal forcing in E4, $\dot{\Theta}_1^{md}$ would be zero and Υ_* would be unity barring subgrid turbulent transport. In practice, the value of Υ_* obtained from 5-min output in a reference frame centered at $\mathbf{x}_{ca}$ is approximately 0.98 ± 0.02 during the intervals $1 \leq t \leq 12$ h and $24 \leq t \leq 30$ h. The condition $\Upsilon_* \approx 1$ distinguishes E4 from E3, and from E1 where during the forcing period $\Upsilon_* = 0.14 \pm 0.08$.

On the other hand, the SSC of E4 is verifiably similar to that of E1. Take the same cylindrical shell used in section C.1 to define the rms and mean values of u_0 and w_0. It is found that u_0^{rms} and w_0^{rms} are respectively 5.7 and 0.7 m s^{-1} in E4, compared to 5.4 and 0.7 m s^{-1} in E1. The means of u_0 and w_0 are 2.4 and 0.36 m s^{-1} in E4, compared to 2.6 and 0.34 m s^{-1} in E1. The preceding statistics are again averages from hourly snapshots taken for $t \leq 35$ h.

As a final remark, the VAP^2 growth rate budget of E4 is fairly similar to that of E1 [Fig. 14a]. In particular, $\tilde{S}_i^1$ provides a significant negative contribution early on that is largely determined by its SSC component. The amplitude of the early negative peak in the time series of $\tilde{S}_{ssc}$ is 0.64 times that of E1, and the duration of the negative peak is approximately 2 h instead of 4 h.

D. Vorticity Profiles and Moisture Parameterizations Used in the SLT

The approximation for ζ used in the SLT to represent the initial vortex in E1-E4 is

$$\begin{aligned}\bar{\zeta}^0 &= \frac{0.0018}{1+(r/107970)^{8.9635}} - \frac{0.0012188}{1+(r/73270)^{4.3684}} - \frac{0.000020257}{1+(r/750000)^{24}} \\ &- \frac{0.0004176}{\exp\left[\left(\frac{r-91000}{12500}\right)^2\right]} + \frac{0.00003502}{\exp\left[\left(\frac{r-174690}{71820}\right)^2\right]} + \frac{0.000019313}{\exp\left[\left(\frac{r-404570}{51718}\right)^2\right]},\end{aligned} \tag{D1}$$

whereas that used to represent the contracted vortex in E1-c and E2-c is

$$\begin{aligned}\bar{\zeta}^c &= \frac{0.0040419}{1+(r/68229)^{6.4}} - \frac{0.0039938}{1+(r/52027)^{4.5407}} + \frac{0.00034098}{1+(r/72074)^{2.4462}} \\ &- \frac{0.000019321}{1+(r/750000)^{24}} + \frac{0.00053033}{\exp\left[\left(\frac{r-80000}{11000}\right)^2\right]}.\end{aligned} \tag{D2}$$

Here, $\bar{\zeta}$ and r are in units of s^{-1} and m, respectively. The analytical functions used to represent the N^2-reduction factors in E1, E3 and E1-c are

$$\Upsilon_b^{E1} = 1 - \frac{0.17505}{1+\left(\frac{r}{340000}\right)^{2.6}} - \frac{0.094295}{\exp\left[\left(\frac{r}{22611}\right)^2\right]} - \gamma\frac{0.3728}{\exp\left[\left(\frac{r-100000}{23107}\right)^2\right]}, \tag{D3}$$

$$\Upsilon_b^{E3} = 1 - \frac{0.428}{1+\left(\frac{r-111670}{139950}\right)^2} - \gamma\frac{0.18484}{\exp\left[\left(\frac{r-111670}{29858}\right)^2\right]}, \quad \text{and} \tag{D4}$$

$$\Upsilon_b^{E1-c} = 1 - \frac{0.14815}{1 + \frac{r}{639190}} + \frac{0.11347}{\exp\left[\left(\frac{r}{60595}\right)^2\right]} - \frac{\gamma}{2\exp\left[\left(\frac{r-82000}{19385}\right)^2\right]}. \tag{D5}$$

The values of γ are given in Table 2.

E. Computation of Complex Quasimode Frequencies

Damped PTMs are not genuine normal modes of the linear system [Eqs. (6)-(8) without forcing], because the damping mechanism requires aberrant growth of perturbation PV in the neighborhood of the critical radius [S02; SM03; SM04]. One practical method for finding the complex frequency of a damped PTM (also known as a quasimode) is to examine the evolution of a quasi-balanced tilt in the absence of forcing. The procedure starts by setting the wavenumber-1 vertical vorticity perturbation ζ' proportional to $\cos(\pi z/H)d\bar{\zeta}/dr$ in the vortex core. The nondivergent component of the horizontal velocity perturbation is made consistent with ζ', whereas the divergent component and w' are set to zero. The geopotential perturbation is initialized such that it zeroes the time derivative of horizontal flow divergence.

Figure A3 illustrates the free evolution of quasi-balanced tilts in vortices with $\bar{\zeta} = \bar{\zeta}^c$ and moisture parameterized as in L1-c1, L1-c2 and L2-c. The plotted variables are the amplitude and phase of the radial velocity wavefunction $\hat{u}(r,t)$, defined by $u' = \hat{u}\cos(\pi z/H)e^{i\varphi} + c.c.$ In all cases, the early behavior of $\hat{u}$ is essentially invariant with radius in the outer core. Moreover, $\hat{u}$ exhibits the exponential decay and constant oscillation frequency characteristic of a damped normal mode. The oscillation frequency and negative growth rate are identified as ω_R and ω_I of the PTM.

References

Antkowiak, A. and P. Brancher, 2004: Transient energy growth for the Lamb-Oseen vortex. *Phys. Fluids*, **16**, L1-L4.

Balmforth, N.J., S.G. Llewellyn Smith, and W.R. Young, 2001: Disturbing vortices. *J. Fluid Mech.*, **426**, 95-133.

Billant, P., and S. Le Dizès, 2009: Waves on a columnar vortex in a strongly stratified fluid. *Phys. Fluids*, **21**, 106602:1-9.

Braun, S.A., M.T. Montgomery and Z. Pu, 2006: High-resolution simulation of hurricane Bonnie (1998). Part 1: The organization of eyewall vertical motion. *J. Atmos. Sci.* , **63**, 19-42.

Braun, S.A., and L. Wu, 2007: A numerical study of Hurricane Erin (2001): Part II: Shear and the organization of eyewall vertical motion. *Mon. Wea. Rev.*, **135**, 1179-1194.

Briggs, R.J., J. D. Daugherty, and R. H. Levy, 1970: Role of Landau damping in crossed-field electron beams and inviscid shear flow. *Phys. Fluids*, **13**, 421-432.

Bryan, G., 2008: On the computation of pseudoadiabatic entropy and equivalent potential temperature. *Mon. Wea. Rev.*, **136**, 5239-5245.

Chen, Y., G. Brunet, and M.K. Yau, 2003: Spiral bands in a simulated hurricane. Part II: Wave activity diagnostics. *J. Atmos. Sci.*, **60**, 1239-1256.

Cotton, W.R., R.A. Pielke Sr., R.L. Walko, G.E. Liston, C.J. Tremback, H. Jiang, R.L. McAnelly, J.Y. Harrington, M.E. Nicholls, G.C. Carrio and J.P. McFadden, 2003: RAMS 2001: Current status and future directions. *Meterol. Atmos. Phys.*, **82**, 5-29.

Davis, C.A., S.C. Jones, and M. Riemer, 2008: Hurricane vortex dynamics during Atlantic extratropical transition. *J. Atmos. Sci.*, **65**, 714-736.

DeMaria, M., 1996: The effect of vertical shear on tropical cyclone intensity change. *J. Atmos. Sci.*, **53**, 2076-2088.

Durran, D.R. and J.B. Klemp, 1982: On the effects of moisture on the Brunt-Väisälä frequency. *J. Atmos. Sci.*, **39**, 2152-2158.

Emanuel, K.A., 1986: An air sea interaction theory for tropical cyclones. Part I: Steady state maintenance. *J. Atmos. Sci.*, **43**, 585-604.

Frank, W.M. and E.A. Ritchie, 2001: Effects of vertical shear on the intensity and structure of numerically simulated hurricanes. *Mon. Wea. Rev.*, **129**, 2249-2269.

Hodyss, D., and D.S. Nolan, 2008: The Rossby-inertia-buoyancy instability in baroclinic vortices. *Phys. Fluids*, **20**, 096602:1-21.

Hoskins, B.J., F.P. Bretherton, 1972: Atmospheric frontogenesis models: mathematical formulation and solution. *J. Atmos. Sci*, **29**, 11-37.

Jones, R.W., Willoughby, H.E., and M.T. Montgomery, 2009: Alignment of hurricane-like vortices on f and β planes. *J. Atmos. Sci.*, **66**, 1779-1792.

Jones, S.C., 1995: The evolution of vortices in vertical shear. I: Initially barotropic vortices. *Q. J. Roy. Meteor. Soc.*, **121**, 821-851.

Jones, S.C., 2000a: The evolution of vortices in vertical shear. II: Largescale asymmetries. *Quart. J. Roy. Meteor. Soc.*, **126**, 3137-3159.

Jones, S.C., 2000b: The evolution of vortices in vertical shear. III: Baroclinic vortices. *Quart. J. Roy. Meteor. Soc.*, **126**, 3161-3185.

Jones, S.C., 2004: On the ability of dry tropical-cyclone-like vortices to withstand vertical shear. *J. Atmos. Sci.*, **61**, 114-119.

Jordan, C.L, 1958: Mean soundings for the West Indies area. *J. Meteorol.*, **15**, 91-97.

Lansky, I.M., T.M. O'Neil and D.A. Schecter, 1997: A theory of vortex merger, *Phys. Rev. Lett.*, **79**, 1479-1482.

Louis, J. F. 1979: A Parametric Model of Vertical Eddy Fluxes in the Atmosphere, *Boundary-Layer Meteorol.*, **17**, 187-202.

Mahrer, Y. and R.A. Pielke, 1977: A numerical study of the airflow over irregular terrain. *Beitrage zur Physik der Atmosphare*, **50**, 98-113.

McWilliams, J.C., L.P. Graves, and M.T. Montgomery, 2003: A formal theory for vortex Rossby waves and vortex evolution. *Geophys. & Astrophys. Fluid Dyn.*, **97**, 275-309.

Möller, J.D. and M.T. Montgomery, 2000: Tropical cyclone evolution via potential vorticity anomalies in a three-dimensional balance model. *J. Atmos. Sci.*, **57**, 3366-3387.

Montgomery, M.T., and R.J. Kallenbach, 1997: A theory of vortex Rossby-waves and its application to spiral bands and intensity changes in hurricanes. *Q. J. Roy. Meteorol. Soc.*, **123**, 435-465.

Montgomery, M.T., and C. Lu 1997: Free waves on barotropic vortices. I. Eigenmode structure. *J. Atmos. Sci.*, **54**, 1868-1885.

Nolan, D.S., and B.F. Farrell, 1999: Generalized stability analysis of asymmetric disturbances in one- and two-celled vortices maintained by radial inflow. *J. Atmos. Sci.*, **56**, 1282-1307.

Nolan, D.S., M.T. Montgomery and L.D. Grasso, 2001: The wavenumber-one instability and trochoidal motion of hurricane-like vortices. *J. Atmos. Sci.*, **58**, 3243-3270.

Patra, R., 2004: Idealised modelling of tropical cyclones in vertical shear: The role of saturated ascent in the inner core. Pre-prints, *26th Conf. on Hurricanes and Tropical Meteorology*, Miami, FL, Amer. Meteor. Soc., 4A.6.

Polvani, L.M., 1991: Two-layer geostrophic vortex dynamics. Part 2: Alignment and two-layer V-states. *J. Fluid Mech.*, **225**, 241-270.

Reasor, P.D., and M.T. Montgomery, 2001: Three-dimensional alignment and co-rotation of weak, TC-like vortices via linear vortex-Rossby-waves. *J. Atmos. Sci.*, **58**, 2306-2330.

Reasor, P.D., M.T. Montgomery, and L.D. Grasso, 2004: A new look at the problem of tropical cyclones in shear flow: vortex resiliency. *J. Atmos. Sci.*, **61**, 3-22.

Reasor, P.D., and M.D. Eastin, 2012: Rapidly intensifying Hurricane Guillermo (1997). Part II: Resilience in shear. *Mon. Wea. Rev.*, **140**, 425-444.

Reasor, P.D., R. Rogers and S. Lorsolo, 2013: Environmental flow impacts on tropical cyclone structure diagnosed from airborne Doppler radar composites *Mon. Wea. Rev.*, **141**, 2949-2969.

Riemer, M., M.T. Montgomery, and M.E. Nicholls, 2010: A new paradigm for intensity modification of tropical cyclones: thermodynamic impact of vertical wind shear on the inflow layer. *Atmos. Chem. Phys.*, **10**, 3163-3188.

Riemer, M., M.T. Montgomery, and M.E. Nicholls, 2013: Further examination of the thermodynamic modification of the inflow layer of tropical cyclones by vertical wind shear. *Atmos. Chem. Phys.*, **13**, 327-346.

Rogers, R., S. Chen, J. Tenerelli and H. Willoughby, 2003: A numerical study of the impact of vertical shear on the distribution of rainfall in hurricane Bonnie (1998). *Mon. Wea. Rev.*, **131**, 1577-1599.

Schecter, D.A., D.H.E. Dubin, A.C. Cass, C.F. Driscoll, I.M. Lansky and T.M. O'Neil, 2000: Inviscid damping of asymmetries on a two-dimensional vortex.*Phys. of Fluids*, **12**, 2397-2412.

Schecter, D.A., M.T. Montgomery, and P.D. Reasor, 2002: A theory for the vertical alignment of a quasigeostrophic vortex. *J. Atmos. Sci.*, **59**, 150-168.

Schecter, D.A., and M. T. Montgomery, 2003: On the symmetrization rate of an intense geophysical vortex. *Dyn. Atmos. Oceans*, **37**, 55-88.

Schecter, D.A., and M.T. Montgomery, 2004: Damping and pumping of a vortex Rossby wave in a monotonic cyclone: critical layer stirring versus inertia-buoyancy wave emission. *Phys. Fluids* **16**, 1334-1348.

Schecter, D.A., and M.T. Montgomery, 2006: Conditions that inhibit the spontaneous radiation of spiral inertia-gravity waves from an intense mesoscale cyclone. *J. Atmos. Sci*, **63**, 435-456.

Schecter, D.A., and M.T. Montgomery, 2007: Waves in a cloudy vortex. *J. Atmos. Sci*, **64**, 314-337.

Schecter, D.A., 2008: The spontaneous imbalance of an atmospheric vortex at high Rossby number. *J. Atmos. Sci.*, **65**, 2498-2521.

Shapiro, L.J., and M.T. Montgomery, 1993: A three-dimensional balance theory for rapidly rotating vortices. *J. Atmos. Sci.* **50**, 3322-3335.

Smagorinsky, J., 1963: General circulation experiments with the primitive equations. *Mon. Wea. Rev.*, **91**, 99-164.

Smith, R.A., and M.N. Rosenbluth, 1990: Algebraic instability of hollow electron columns and cylindrical vortices. *Phys. Rev. Lett.*, **64**, 649-652.

Tang, B., and K. Emanuel, 2010: Mid-level ventilation's constraint on tropical cyclone intensity. *J. Atmos. Sci.*, **67**, 1817-1830.

Vandermeirsh, F., Y.M. Morel and G. Sutyrin, 2002: Resistance of a coherent vortex to a vertical shear. *J. Phys. Ocean.*, **32**, 3089-3100.

Viera, F., 1995: On the alignment and axisymmetrization of a vertically tilted geostrophic vortex. *J. Fluid Mech.*, **289**, 29-50.

Walko, R.L., W. R. Cotton, M. P. Meyers, and J. Y. Harrington, 1995: New RAMS cloud microphysics parameterization. Part 1: The single-moment scheme. *Atmos. Res.*, **38**, 29-62.

Walko, R.L., L.E. Band, J. Baron, T.G.F. Kittel, R. Lammers, T.J. Lee, D. Ojima, R.A. Pielke Sr., C. Taylor, C. Tague, C.J. Trembeck and P.L. Vidale, 2000: Coupled atmosphere-biophysics-hydrology models for environmental modeling. *J. App. Meteor.*, **39**, 931-944.

Wang, Y., and G. J. Holland, 1996: Tropical cyclone motion and evolution in vertical shear. *J. Atmos. Sci.*, **53**, 3313-3332.

Wong, M.L.M., and J.C.L. Chan, 2004: Tropical cyclone intensity in vertical wind shear. *J. Atmos. Sci.*, **61**, 1869-1876.

Zhang, D.L., and C.Q. Kieu, 2006. Potential vorticity diagnostics of a simulated hurricane. Part II: Quasi-balanced contributions to forced secondary circulations. *J. Atmos. Sci.*, **63**, 2898-2914.

Zhang, F. and D. Tao, 2013: Effects of vertical wind shear on the predictability of tropical cyclones. *J. Atmos. Sci.*, **70**, 975-983.

Experiment	Initialization	Moisture	Surface Fluxes	Radiation
E1, E1-c	moist convective hurricane	vapor, cloud droplets and rain	all activated	longwave
E2, E2-c	dry baroclinic nonconvective vortex	nonexistent	deactivated	deactivated
E3	cloudy baroclinic nonconvective vortex	vapor and suspended cloud droplets	deactivated	deactivated
E4	dry baroclinic convective vortex	artificial axisymmetric heating	momentum only	deactivated

TABLE 1. Brief description of the CM experiments. The initial vortices in E2-E4 are designed to resemble the initial hurricane in E1. The initial vortices in E1-c and E2-c are modeled after a slightly contracted state of the hurricane found late in E1.

version label	corresponding CM experiment	$\bar{\zeta}$	Υ_b	γ
L1-1	E1	$\bar{\zeta}^0$	Υ_b^{E1}	1
L1-2	E1	$\bar{\zeta}^0$	Υ_b^{E1}	2.2
L2	E2	$\bar{\zeta}^0$	1	—
L3-1	E3	$\bar{\zeta}^0$	Υ_b^{E3}	1
L3-2	E3	$\bar{\zeta}^0$	Υ_b^{E3}	2
L1-c1	E1-c	$\bar{\zeta}^c$	Υ_b^{E1-c}	1
L1-c2	E1-c	$\bar{\zeta}^c$	Υ_b^{E1-c}	1.4
L2-c	E2-c	$\bar{\zeta}^c$	1	—

TABLE 2. Versions of the linear model relevant to the CM experiments. Each version is defined by its basic state vorticity $\bar{\zeta}$ and static stability reduction profile Υ_b, which depends on the dimensionless parameter γ.

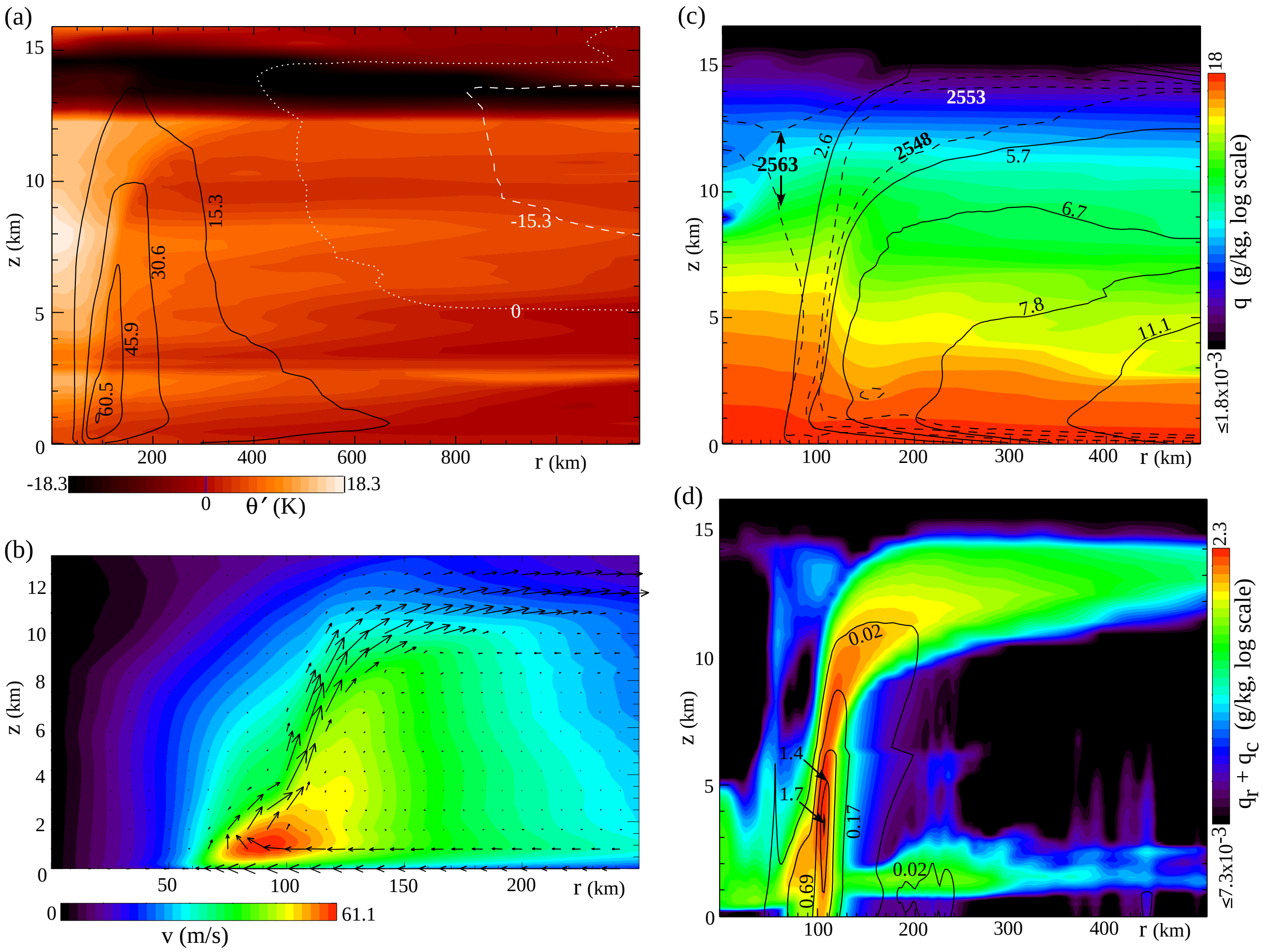

Figure 1: Axisymmetric initial condition of the primary hurricane in E1. (a) Azimuthal velocity v (contours in m s^{-1}) and perturbation potential temperature (red shading). (b) Secondary circulation [(u, w) flow vectors] superposed on a color contour plot of v. The w component of the flow vector is magnified by a factor of 10 relative to u. (c) Saturated pseudoadiabatic entropy (dashed) and absolute angular momentum (solid) contours superposed on a color contour plot of the water vapor mixing ratio q. The entropy and angular momentum contour labels are in units of J kg^{-1}K^{-1} and 10^6 m^{2}s^{-1}, respectively. (d) Mixing ratios of total condensate (color) and rain (contours in g/kg).

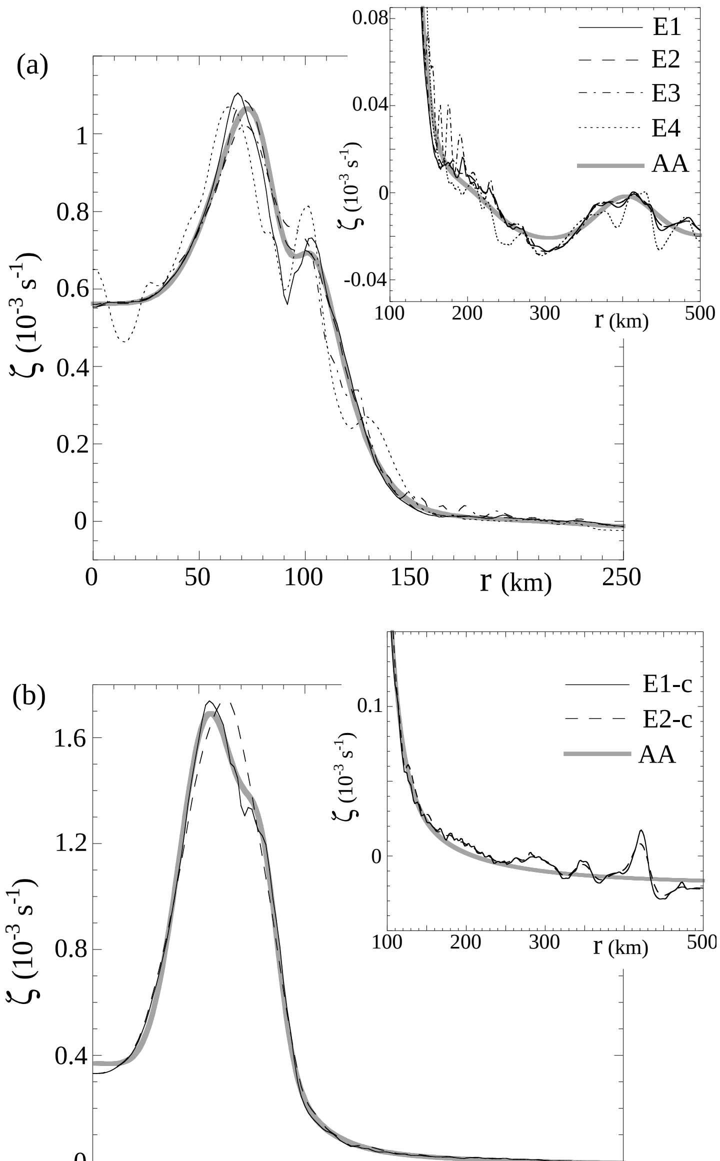

Figure 2: (a) Initial vertical relative vorticity (ζ) profiles for E1-E4, averaged with mass-weighting between $z = 30$ m and 12.3 km. The inset shows details of the outer skirt. The thick gray curve is an analytic approximation (AA) used for the SLT of section 3. (b) Same as (a) but for E1-c and E2-c.

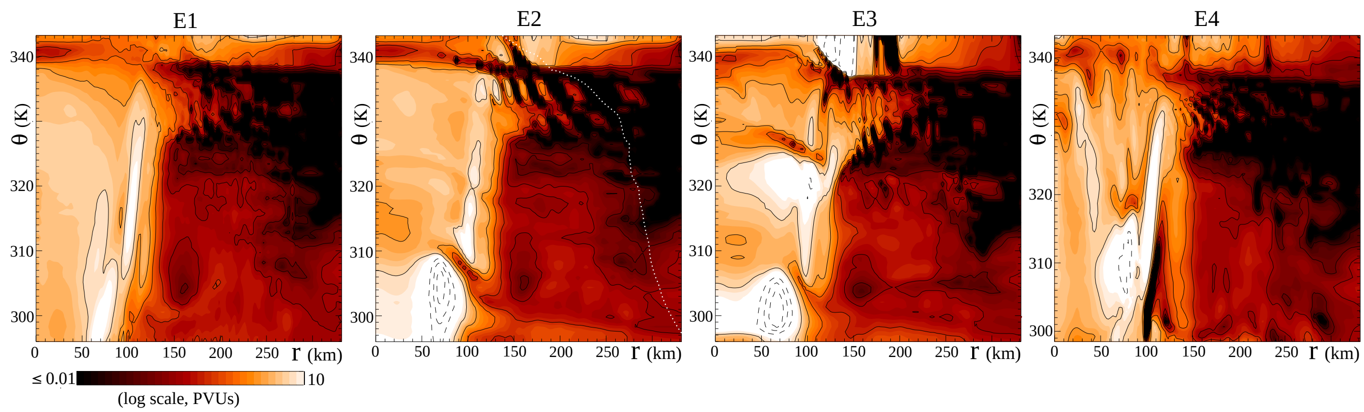

Figure 3: Initial dry isentropic PV distributions for E1-E4 (as labeled). The red color scale is logarithmic and the same for each plot. The solid contours are evenly spaced in $\log(\mathrm{PV}_\theta)$ with the highest two levels corresponding to $\mathrm{PV}_\theta = 6.5$ and 2.7 PVUs. The dashed contours correspond to $\mathrm{PV}_\theta = 20$, 30, and 40 PVUs, with the lowest value belonging to the outermost contour of a nested set. The white dotted curve shows the estimated critical layer of the dry PTM in E2 (described in section 4.2).

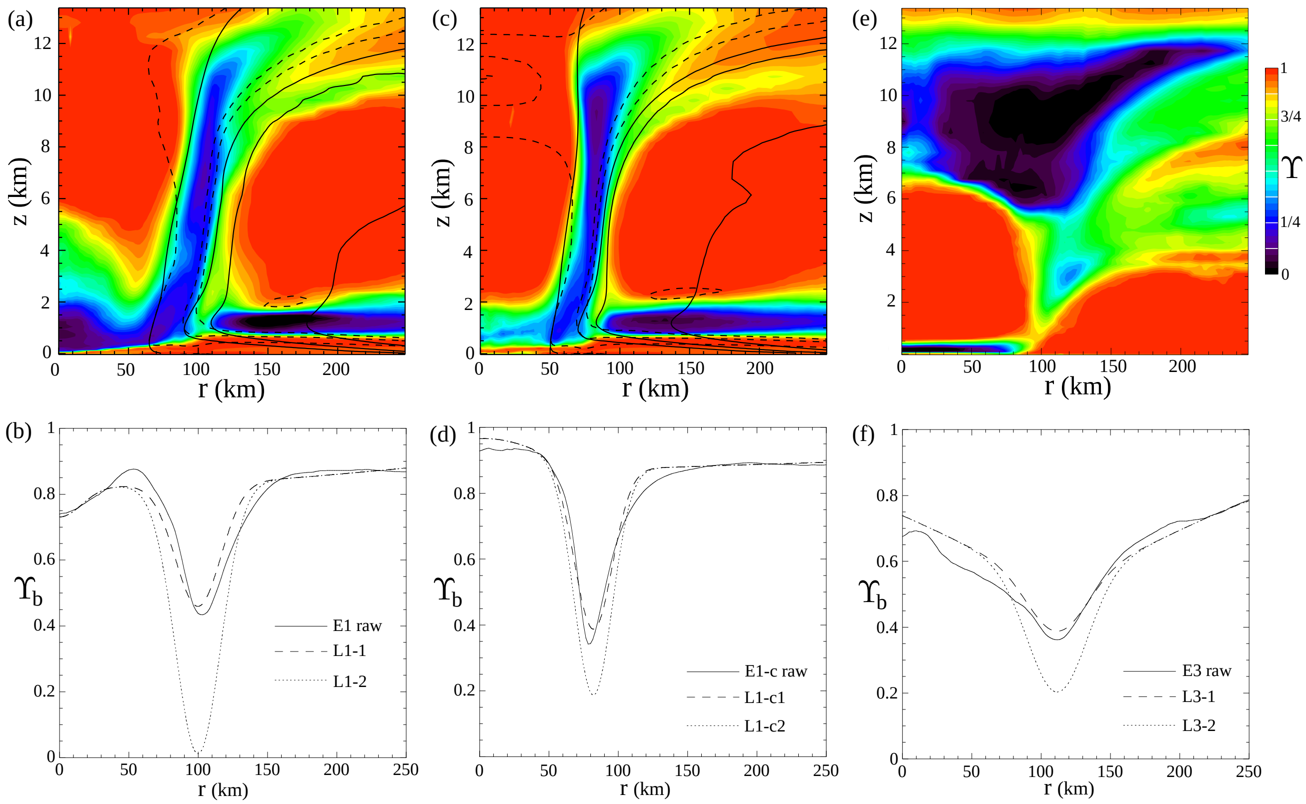

Figure 4: Theoretical estimates for the reduction of static stability. (a,c,e) The N^2-reduction factor Υ of SM07 for (a) the primary hurricane in E1, (c) the contracted hurricane in E1-c, and (e) the cloudy vortex in E3. The solid and dashed curves in (a) and (c) are contours of absolute angular momentum and saturated pseudoadiabatic entropy, respectively. (b,d,f) The vertical averages of Υ (solid curves) for (b) the primary hurricane in E1, (d) the contracted hurricane in E1-c, and (f) the cloudy vortex in E3. The dashed and dotted curves are the analytic N^2-reduction factors used for the indicated versions of the SLT.

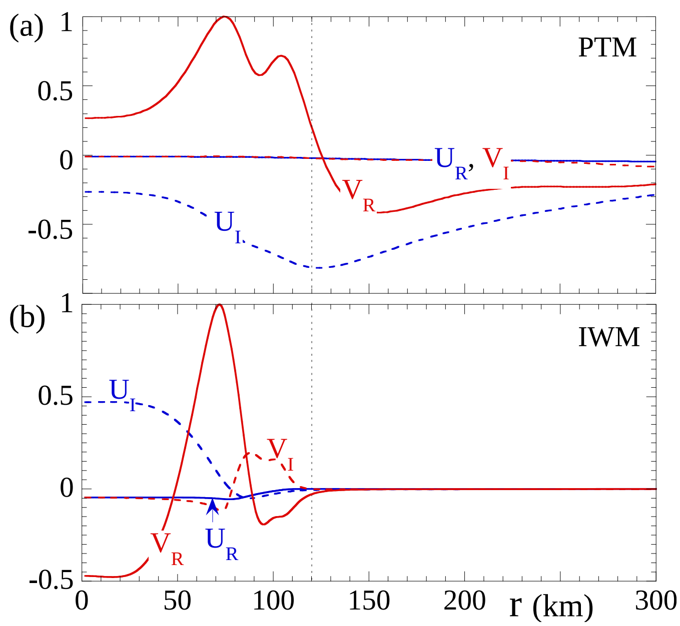

Figure 5: Theoretical wavefunctions for (a) the PTM and (b) the IWM of the dry barotropic vortex in L2, whose vorticity distribution [Eq. (D1)] is modeled after that in E1-E4. Red and blue curves respectively correspond to the azimuthal velocity (V) and radial velocity (U). Solid and dashed curves respectively correspond to the real part (subscript R) and imaginary part (subscript I) of the wavefunction. In both (a) and (b) the wavefunctions are normalized to the peak value of V_R. The vertical dotted line is at the RMW, which exceeds that near the base of the vortices in E1-E4 owing to the vertical averaging used to obtain $\bar{\zeta}$.

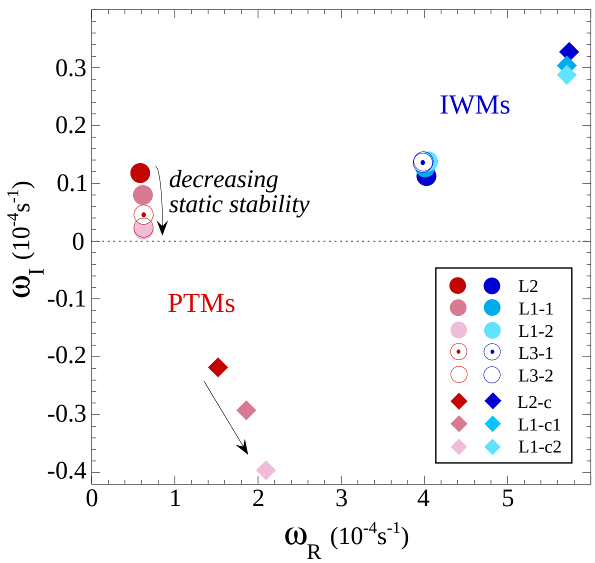

Figure 6: Complex frequencies of the PTMs (red) and IWMs (blue) for vortices whose barotropic basic states are modeled after those found in the CM experiments. The legend shows the version of the linear model corresponding to each data point. The arrows near the PTM data sets point in the direction of decreasing static stability in the vicinity of the eyewall.

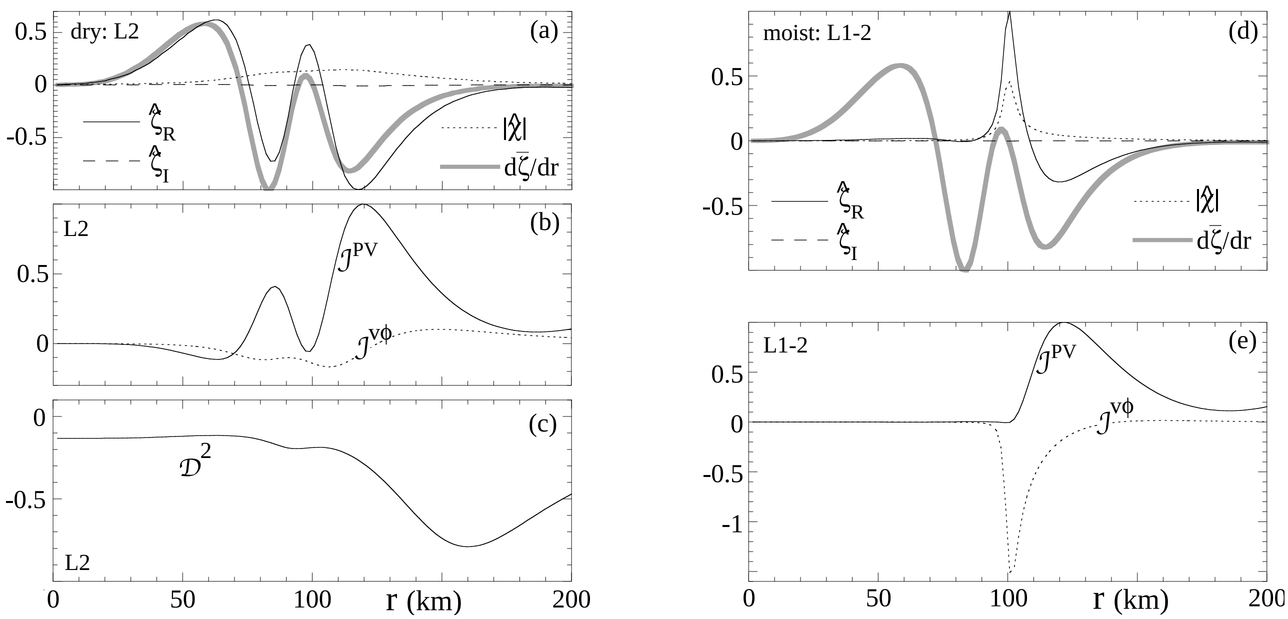

Figure 7: Comparison of the PTM of the dry vortex of L2 to the PTM of the same vortex with moisture parameterized as in L1-2. (a) Snapshots of $\hat{\zeta} \equiv \hat{\zeta}_R + i\hat{\zeta}_I$ and $|\hat{\chi}|$ for the dry PTM in L2. Both fields are normalized to the peak magnitude of $\hat{\zeta}_R$. The thick gray curve shows $d\bar{\zeta}/dr$ normalized to its peak magnitude. (b) The PV and $v\phi$ components of angular pseudomomentum for the PTM of the dry vortex in L2, normalized to the instantaneous peak value of $\mathcal{J}^{PV}$ in the vortex core. (c) The asymmetric balance parameter $\mathcal{D}^2$ of the PTM of L2. (d,e) Same as (a,b) but for the moist PTM of L1-2. The bottom radial axis labels apply to all plots in the column.

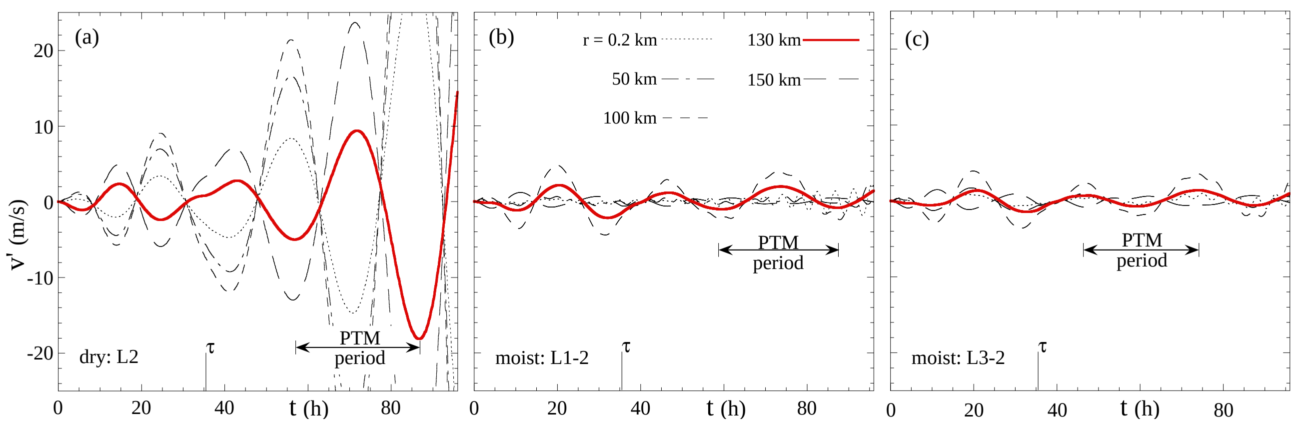

Figure 8: (a) Time series of the azimuthal velocity perturbation (v') generated by misalignment forcing [Eq. (5)] in the dry vortex of L2. The time series are taken at $z = 0$, $\varphi = 0$ and various r. The thick red curve corresponds to a radius just outside the RMW. The end of the forcing period is marked by τ on the bottom axis. The double-arrowed line segment shows the natural wave period of the PTM. (b) Same as (a) but with the L1-2 moisture parameterization added to the vortex. (c) Same as (a) but with the L3-2 moisture parameterization added to the vortex. The legend in (b) applies to all plots.

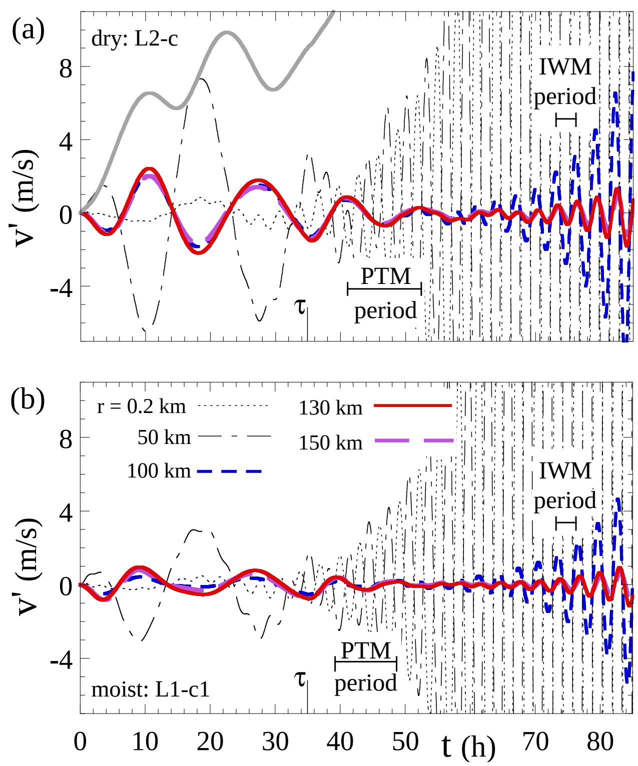

Figure 9: Linear response of the contracted vortex to misalignment forcing. (a,b) The azimuthal velocity perturbation (v') at $z = 0$ and $\varphi = 0$ generated in (a) the dry vortex of L2-c and (b) the moist vortex of L1-c1. The legend in (b) also applies to (a). For reference, the thick gray curve in (a) shows the maximum amplitude of v' (at $z = 0$ and the plotted values of r) in the response of the primary vortex of L2 [Fig. 8a].

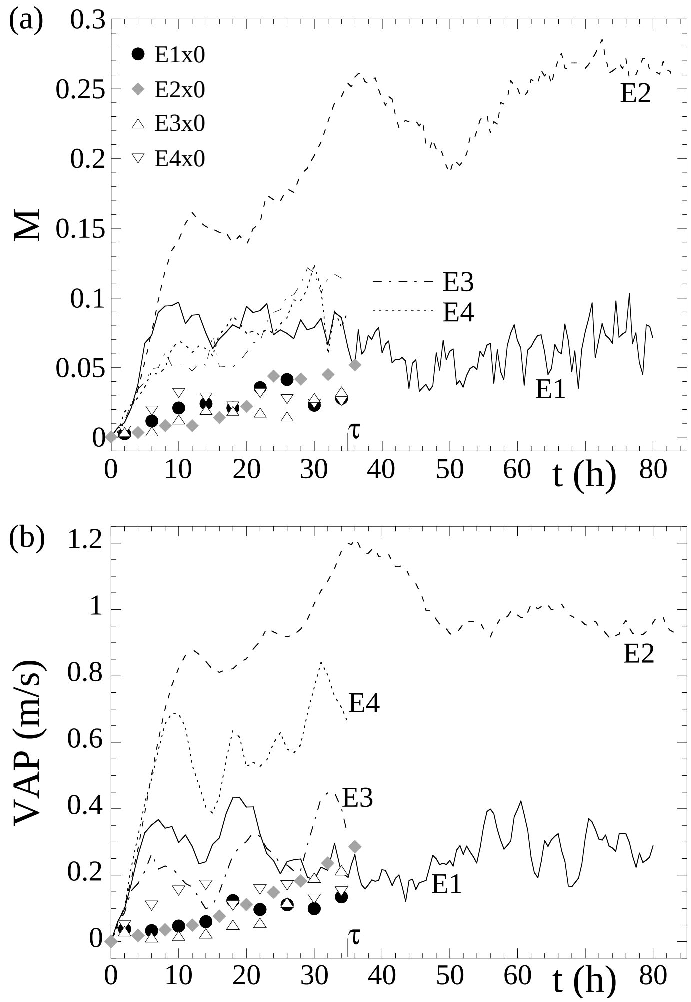

Figure 10: Evolution of misalignment and VAP in the main CM experiments. (a) Time series of M in E1-E4 and in a set of complementary experiments (E1-E4$\times$0) without applied forcing. (b) Similar time series of VAP.

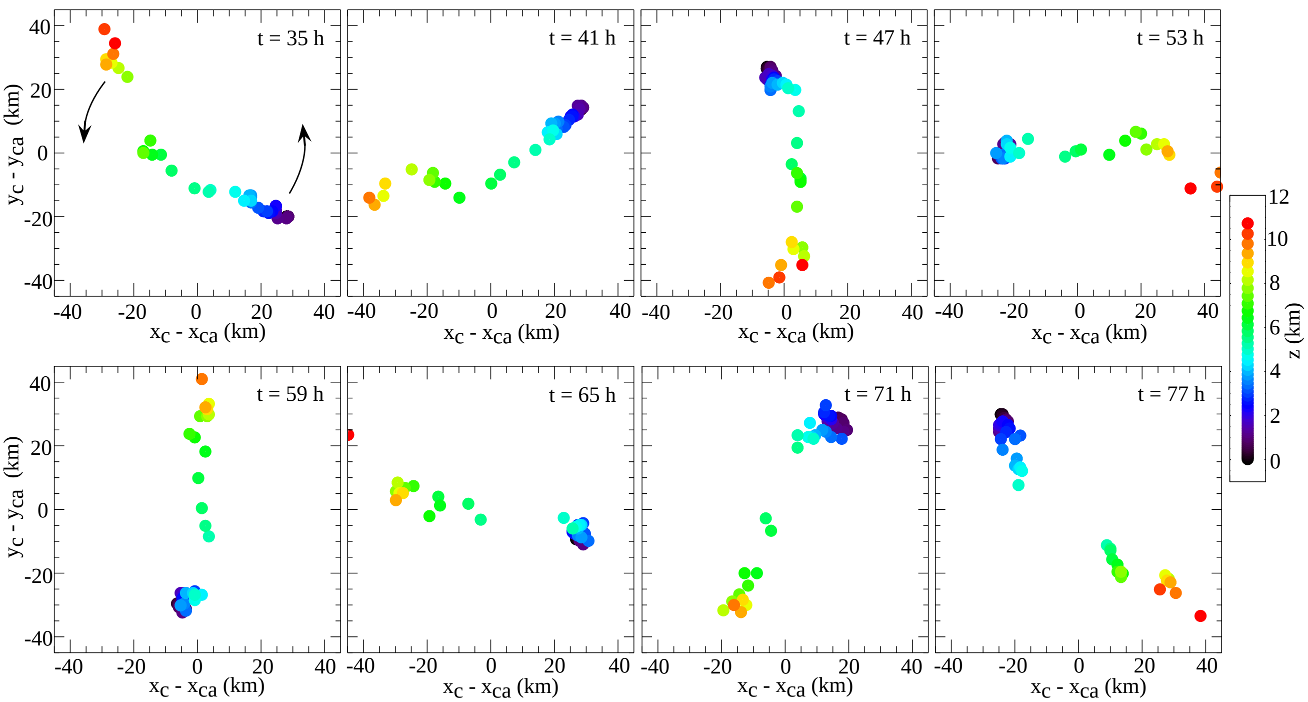

Figure 11: Snapshots of the rotational centers during the free evolution of the dry vortex in E2. Different colors correspond to different altitudes, as indicated in the legend to the right. The snapshots show clear evidence of a rotating tilt mode.

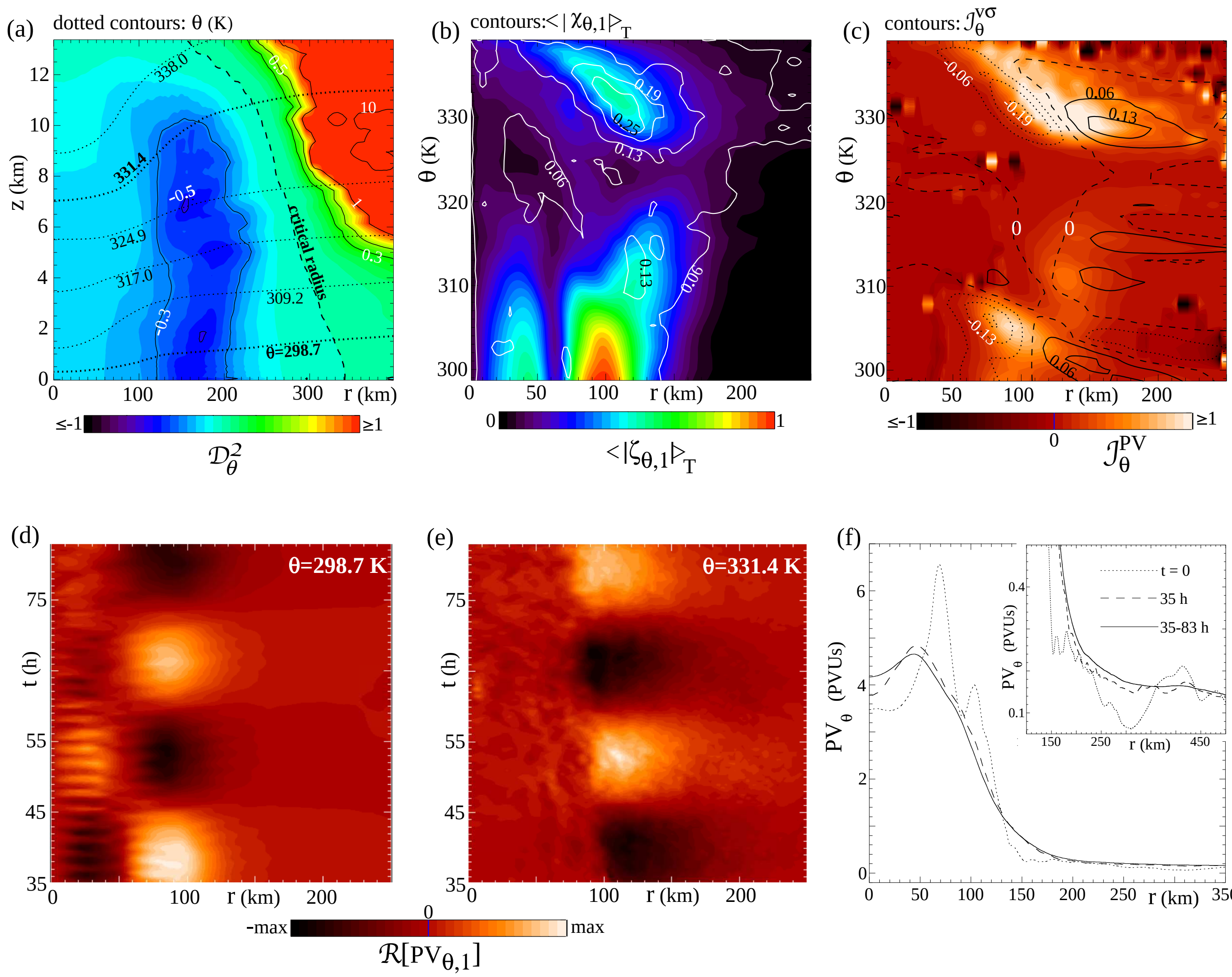

Figure 12: PTM of the dry vortex in E2. (a) Contour plot of the asymmetric balance parameter $\mathcal{D}_\theta^2$ of the PTM in the r-z plane. The dashed curve corresponds to the z-dependent critical radius of the PTM, where $\mathcal{D}_\theta^2 = 0$. The dotted curves are θ-contours shown to assist the reader in relating the (r, θ) coordinates of (b) and (c) to (r, z). (b) Time-averaged amplitudes of the wavenumber-1 relative vorticity (color) and divergence (contours). Both the vorticity and divergence amplitudes are normalized to the maximum of $\langle|\zeta_{\theta,1}|\rangle_T$. (c) The PV component (red shading) and $v\sigma$ component (contours) of wavenumber-1 angular pseudomomentum. Both components are given in the same dimensionless units. Solid/dashed/dotted contours correspond to positive/zero/negative values of $\mathcal{J}_\theta^{v\sigma}$. The small bright and dark spots are presumably unimportant and occur where $\partial_r \overline{\mathrm{PV}}_\theta^s$ is exceptionally small. The fields in both (b) and (c) are smoothed with 8-km radial boxcar averaging. (d,e) Hovmöller diagrams of $\Re[\mathrm{PV}_{\theta,1}(r, \theta, t)]$ at (d) $\theta = 298.7$ K and (e) $\theta = 331.4$ K. In both (d) and (e), the plotted fields are normalized to their r-t maxima. (f) Basic-state PV_θ at $t = 0$ (dotted curve), $t = 35$ h (dashed curve) and during the free evolution period (solid curve). The distributions are averaged with σ-weighting over the interval $296 \leq \theta \leq 344$ K.

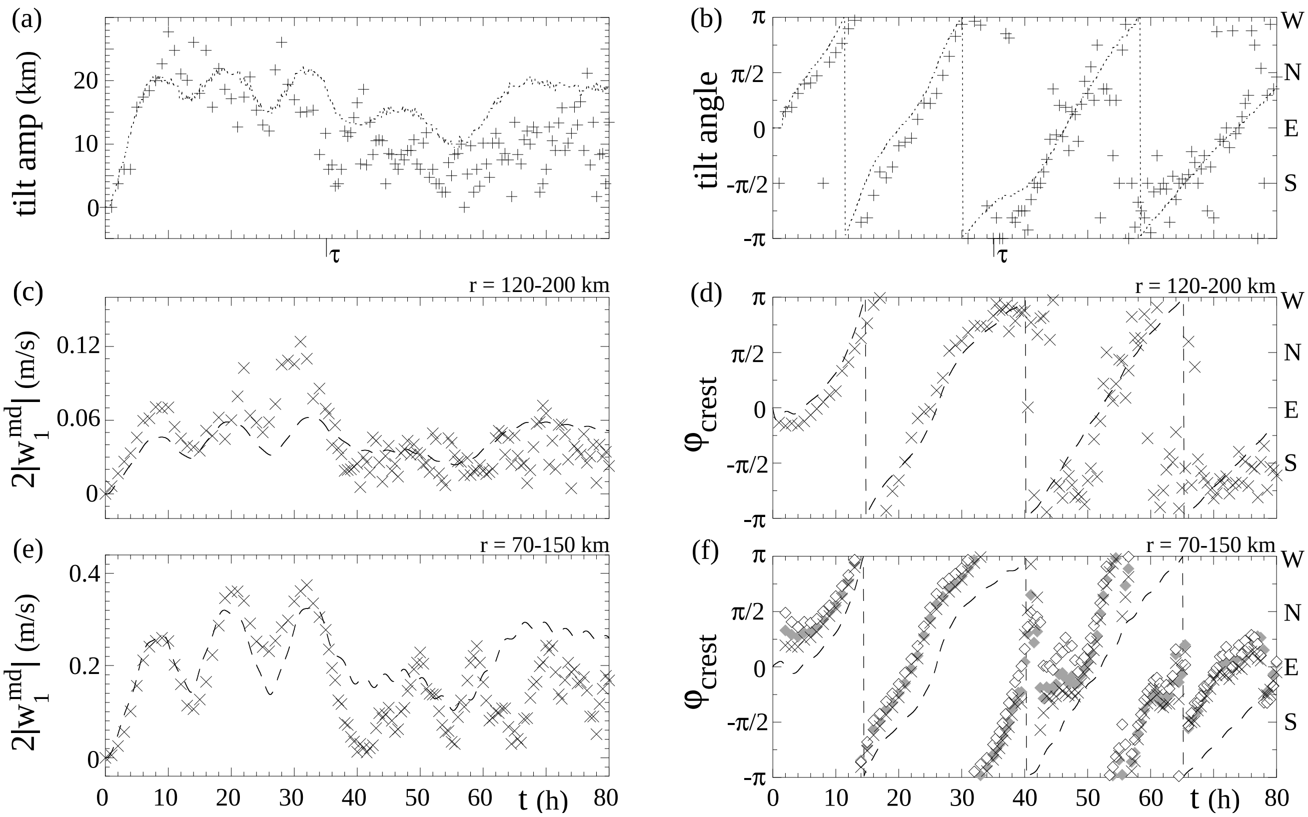

Figure 13: Comparison of the moist tilt dynamics of E1 to that of the SLT with L1-2 specifications. (a,b) Time series of (a) the tilt amplitude and (b) the tilt orientation angle. The +s correspond to E1, whereas the dotted curves correspond to the SLT. (c,d) Time series of (c) the crest amplitude and (d) the crest azimuth of the wavenumber-1 component of midlevel vertical velocity averaged between $r = 120$ and 200 km. The ×s correspond to E1, whereas the dashed curves correspond to the SLT. (e,f) Same as (c,d) but with averaging between $r = 70$ and 150 km so as to include the eyewall region of E1. The crest azimuths of the wavenumber-1 midlevel heating rate (gray diamonds) and column integrated rain-mass (white diamonds) are also shown in (f). The bottom t-axis labels apply to all plots in the column.

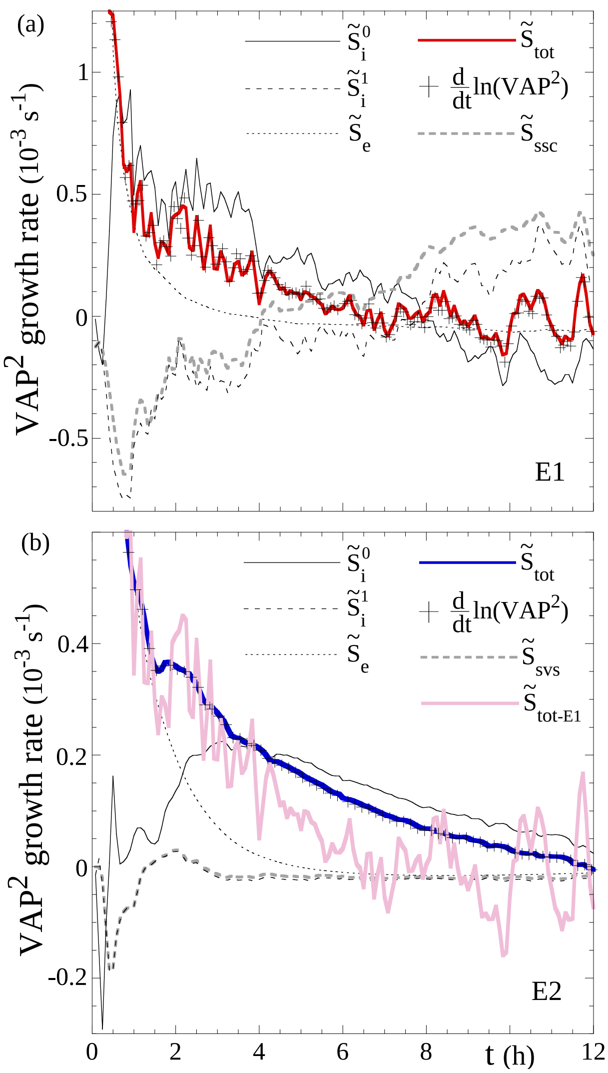

Figure 14: Time series of the VAP^2 growth rate and its components during the first 12 h of misalignment forcing. (a) Results for the moist convective hurricane in E1. The thick red curve is the theoretical growth rate ($\tilde{S}_{tot}$) given by the sum of the solid, dashed and dotted black curves ($\tilde{S}_i^0 + \tilde{S}_i^1 + \tilde{S}_e$). The dashed gray curve is the dominant SSC component of $\tilde{S}_i^1$. The +s show the growth rate obtained from the times series of VAP^2 that is output by the model. (b) Results for the dry nonconvective vortex in E2. Here $\tilde{S}_{tot}$ is given by the thick blue curve, and the dashed gray curve is the component of $\tilde{S}_i^1$ connected to symmetric vertical wind shear. The total growth rate in E1 ($\tilde{S}_{tot-E1}$; thick pink curve) is superposed on the plot to illustrate its lesser value (for the most part) after 4 h of forcing.

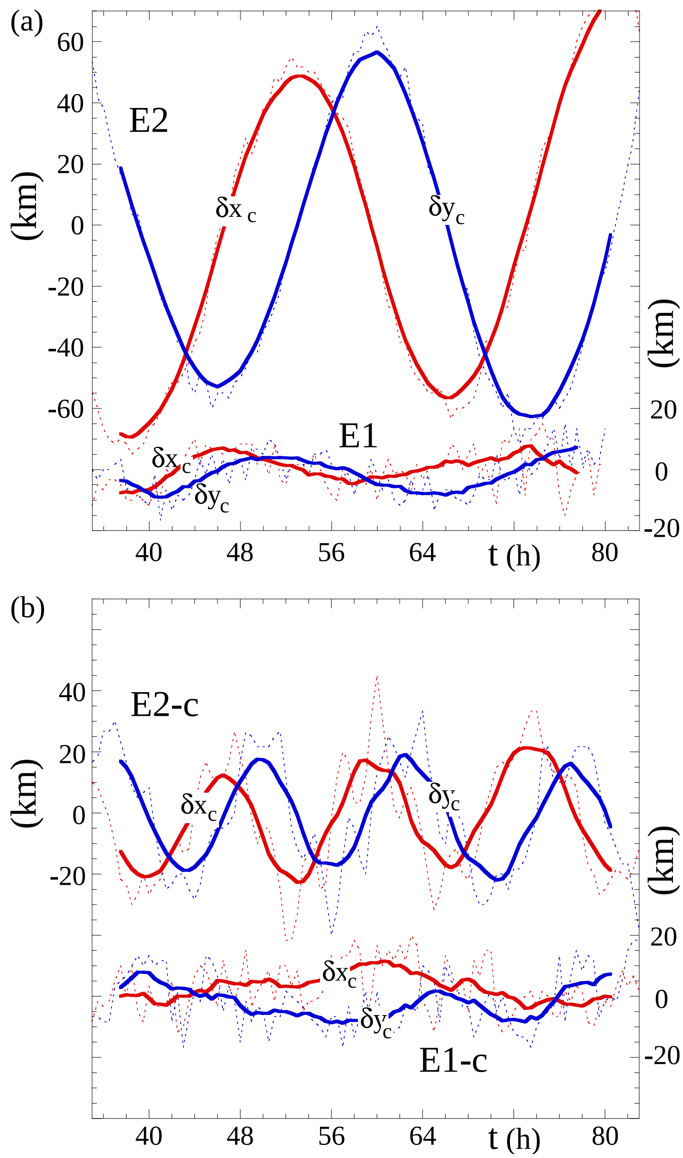

Figure 15: Evolution of the tilt vector ($\delta\mathbf{x}_c \equiv \delta x_c\hat{\mathbf{x}} + \delta y_c\hat{\mathbf{y}}$) after forcing in (a) the primary vortex and (b) the contracted vortex. (a) Time series of δx_c and δy_c in (bottom) the primary hurricane of E1 and (top) its dry analogue in E2. Red and blue curves respectively show δx_c and δy_c. Dotted curves show unfiltered time series, whereas thick solid curves show time series smoothed with 5-h boxcar averaging. (b) Same as (a) but for (bottom) the contracted hurricane of E1-c and (top) its dry analogue in E2-c.

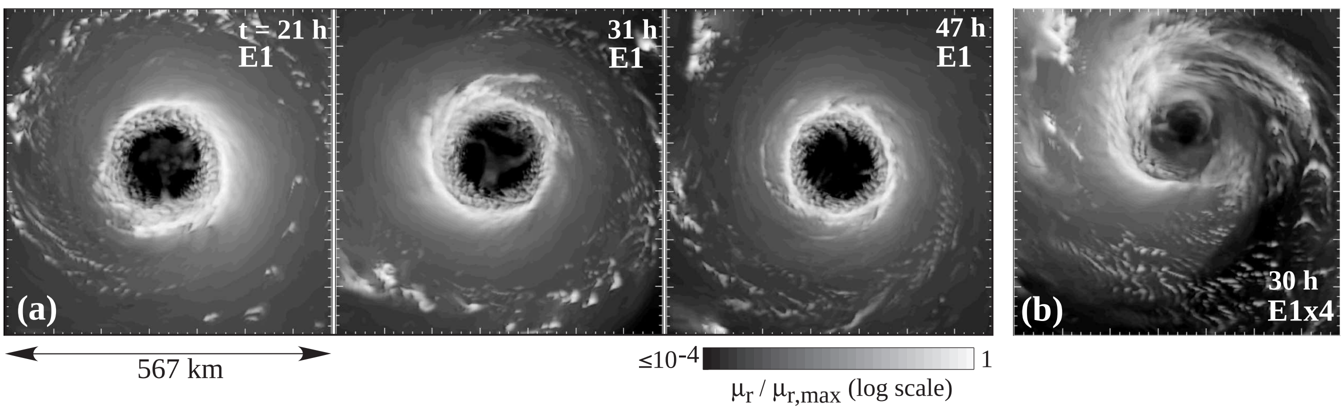

Figure 16: (a) Three snapshots of column integrated rain mass density μ_r normalized to its instantaneous maximum in E1. (b) Select snapshot of normalized μ_r in E1×4.

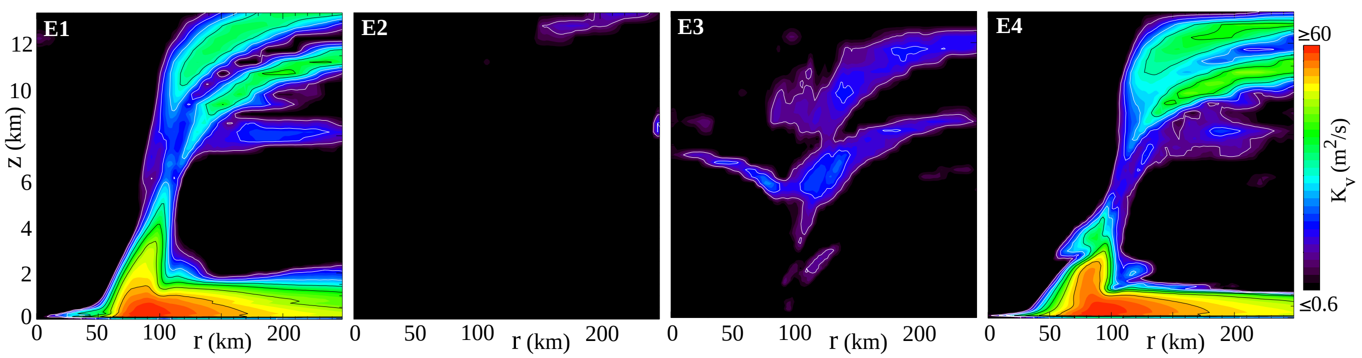

Figure 17: Vertical mixing coefficients averaged over φ and over time during the forcing periods of (left to right) E1, E2, E3 and E4. The color scale is logarithmic and the same for all plots. The contours are evenly spaced in $\log(K_v)$ with the black-to-white transition occurring between the black contour at $K_v = 6$ m^{2}s^{-1} and the white contour at $K_v = 3.4$ m^{2}s^{-1}.

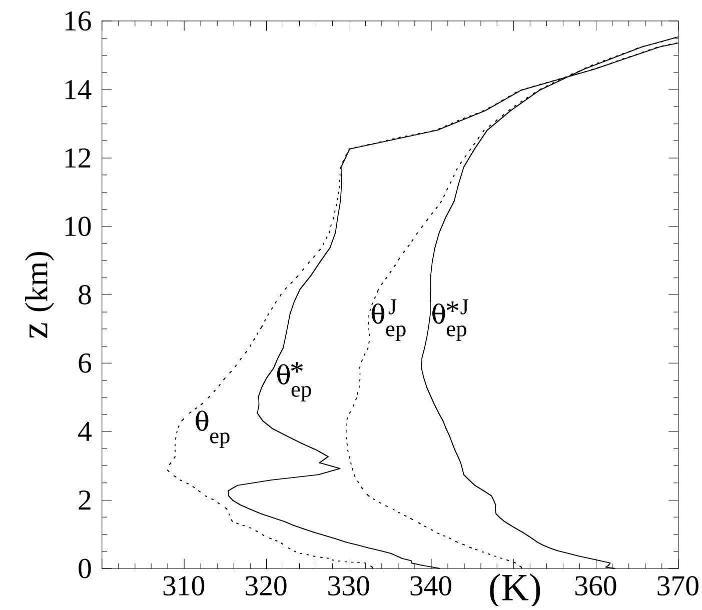

Figure A1: Initial domain-averaged profiles of actual and saturated pseudoequivalent potential temperature (θ_{ep} and θ^*_{ep}) compared to those of the Jordan mean sounding (θ^J_{ep} and θ^{*J}_{ep}).

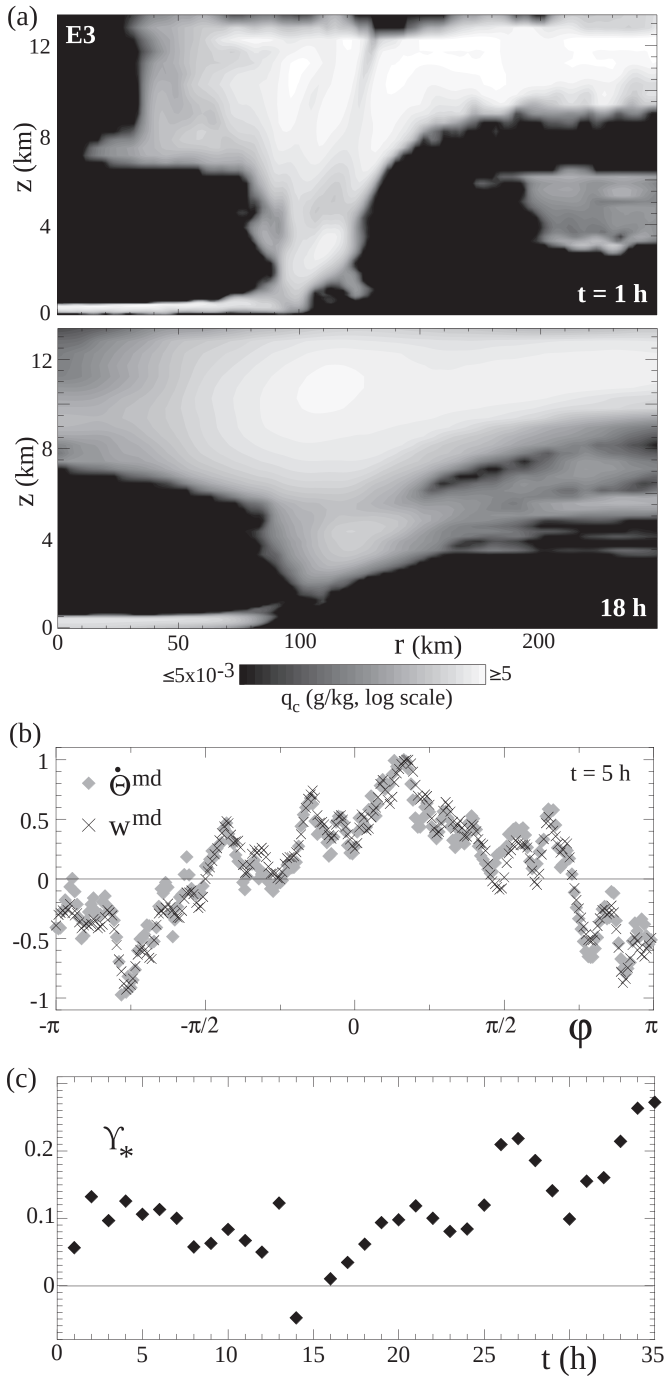

Figure A2: The non-precipitating cloudy vortex of E3. (a) Snapshots of the azimuthally averaged cloud droplet mixing ratio q_c during the application of misalignment forcing. The upper and lower plots respectively correspond to $t = 1$ and 18 h. (b) Typical snapshot of $\dot{\Theta}^{md}$ and w^{md} normalized to their instantaneous peak values. (c) Time series of Υ_*.

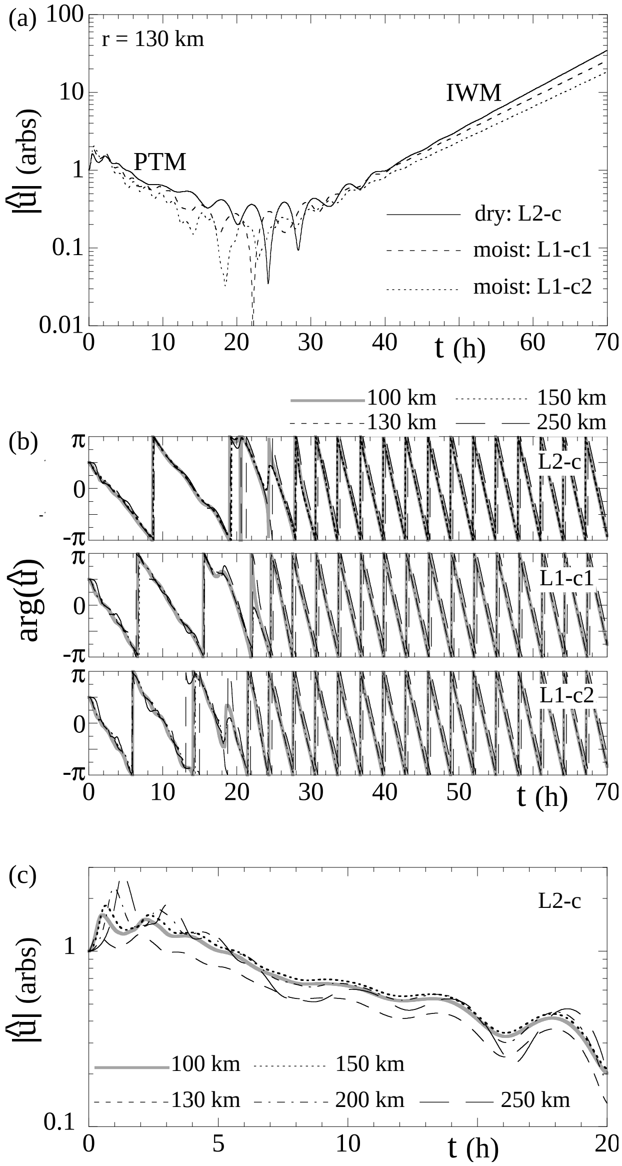

Figure A3: Radial velocity perturbation in an unforced but initially tilted vortex with $\bar{\zeta} = \bar{\zeta}^c$. (a) Time series of the amplitude of $\hat{u}$ at $r = 130$ km for linear simulations with 3 different moisture parameterizations. (b) Time series of the phase of $\hat{u}$ at various outer core radii whose values are shown in the legend. The top plot in (b) corresponds to the dry vortex of L2-c, whereas the middle and bottom plots in (b) respectively correspond to the moist vortices of L1-c1 and L1-c2. (c) Early time series of $|\hat{u}|$ in the dry vortex of L2-c at various outer core radii. All amplitudes in (a) and (c) are normalized to their initial values. Although the skirt of an unstable IWM eventually dominates, a slow exponentially damped quasimode (the PTM) apparently controls the outer perturbation at early times.